Correlation of microstructural damage to functional properties of irradiated carbon fibre based composites used in neutron chopper discs

Master's Dissertation by

Hanna Molin

Abstract

Understanding material behaviour has in the past enabled human development and will continue to characterize the various stages of our future development. The use of neutrons will greatly affect several research areas, such as sustainable energy production and cancer research, due to their interaction with nuclei. Neutrons will thus interact differently depending on the specific isotope, reveal information on crystal and magnetic structure and track dynamics of atoms.

The European Spallation Source is currently under construction and can be compared to a giant powerful neutron microscope which is a huge step forward in everyday life science. To meet the need of each research area, numerous techniques and methodologies are required. To optimize performance, different energy spectra of the neutrons are needed depending on the research area. A neutron chopper is a type of mechanical neutron filter which filters out the wanted energy spectra. One of the most crucial components of the neutron chopper is the disc, made of carbon fibre reinforced epoxy, which will be in contact with the neutron beam. It is thus necessary to analyse the impact of radiation on the neutron chopper disc.

To investigate whether the radiation damage is universal between different types of epoxy, two different epoxy resins were used. Each type of composite was then irradiated with 0, 3, 10 and 30 MGy. Using X-ray tomography in combination with a porosity analysis it was seen that the number of pores increased with radiation dose. However, this effect was only seen in one of the composites meaning that the radiation damage is not universal between different types of epoxy. It was seen that more elliptic medium sized pores are favourable. However, the mechanical properties, tested using three-point bending, showed no apparent change after exposures. Scanning electron microscopy revealed no evident changes of the fracture surfaces after irradiation. In totality, the results helped ESS to confidently select the type of epoxy that will ensure the longest neutron chopper disc lifetime and highest neutron instrument availability.

Acknowledgements

Abbreviations

CCD   -   Charged-Coupled Device

CFR   -   Carbon Fibre Reinforced

CFRP -   Carbon Fibre Reinforced Polymer

ESS   -   European Spallation Source

NDT   -   Non-Destructive Testing

PMC   -   Polymer Matrix Composite

SEM   -   Scanning Electron Microscope

Table of Contents

1. Introduction

Throughout the ages, humans have always been curious of materials. Ages have even been named directly after the materials mankind used; the stone, bronze, and iron ages. To this day, materials have enabled human development and will continue to characterize the various stages of our development in the future. As our knowledge increased, often via trial-and-error processes, we learnt how to produce tougher ceramics and stronger metal alloys. In the 19th century, the thermodynamics helped us understand the concept of a phase and helped us think about the connection between the properties of the materials and the arrangements of the constituting atoms. However, the techniques for analysing the atomic structure was not accomplished until Bragg, von Lau, and Röntgen contributed with X-ray tools [1, p.12].

Although X-rays have been used in great extent to analyse various materials, the use of nuclear started emerging in the 20th century and brought along new possibilities. The neutron was discovered in 1932 by Chadwick, and the work of Bert Brockhouse and Cliff Shull showed that neutrons diffracted just as easily as X-rays. In addition, neutrons can not only reveal information about the crystal structure, but also track the dynamics of atoms and report on magnetic structure. Furthermore, neutrons are scattered by the nuclei and thus scattering depends on the specific isotope and not only the element. Also, using neutrons thus allows for deep penetration of a material [1, pp. 12-14].

1.1. Why is the Neutron Chopper Important?

Neutron scattering can be applied to numerous scientific fields; geology, physics, chemistry, medicine, and biology. It obtains deeper understanding of material behaviour. The European Spallation Source can be compared to a giant microscope for studying various materials -from pharmaceuticals and plastics, to engines, nanotechnology, molecules, and proteins. Hence, ESS is a huge step forward in everyday life science [2]. Some examples of areas where neutrons are very useful are;

Green energy: Solar cells, batteries, and fuel cells are investigated to enable a sustainable energy production. However, the fuel cells are currently limited by cost and performance. Since ESS enables in situ studies, the fuel cell can be imaged during working conditions to better understand how to increase efficiency. Moreover, more detailed information on the structure of materials can be revealed using neutrons [1, p.15].

Treating cancer: When treating cancer, it is not only crucial that the drug is delivered to the tumour, but it must also avoid the healthy tissue. These drug delivery systems need to be observed on a nanoscale to investigate how the drug penetrates the tumour plasma membrane. Thus, the ESS facility would be of great use since neutron scattering would be a suitable technique [1, p.17].

These diverse examples illustrate that numerous techniques and methodologies are required. Thus, 22 instruments are currently being developed to meet the need of each research area. Hence, different instrument classes such as *powder diffraction* and *imaging* have been defined. Depending on the instrument class, different energy spectra are needed to optimize performance [1, pp. 19, 21, 46], see Figure 1.1. Therefore, neutron choppers, a type of mechanical neutron filter, are required. It is thus necessary to investigate how radiation will affect the choppers.
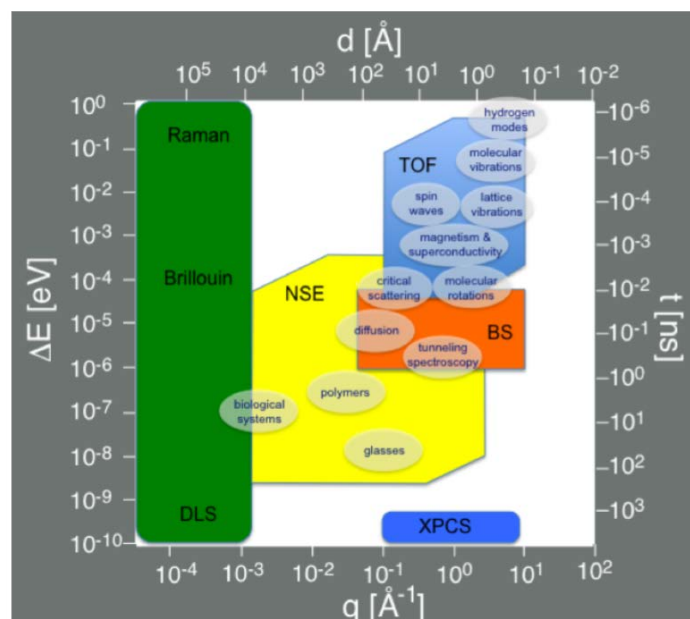
Figure 1.1. Illustrating how different wavelengths are suitable for different experiments. Image taken from [1].

2. Objective

By 2025 the engineering team at the European Spallation Source in Sweden will be responsible for the maintenance of 50 neutron chopper systems which will be operating under high radiation levels. Therefore, it is necessary to examine the potential radiation effect on the most fundamental component of high-performance choppers; the carbon fibre reinforced polymer (CFRP) based disc.

The central aim of this thesis is to:

1. Understand the microstructural mechanism of radiation damage on carbon fibre reinforced polymer (CFRP) based discs that are used in neutron choppers, *and*

2. Investigate whether this mechanism is universal between CFRP composites made with different types of resins.

Gaining insights to where and how the damage initiates, how it propagates and its macroscopic effect on the mechanical properties of the CFRP will greatly enhance the ability to select the correct resin, provide recommendations on the manufacturing technique and allow estimation of CFRP disc lifetime at ESS at a given irradiation environment.

3. Theoretical Background

3.1. The Importance of Choppers at ESS

To comprehend the main objectives of this thesis, it is necessary to understand the need for neutron choppers, and their function. It is thus important to have some background knowledge of ESS. A critical component for ESS is the *linac,* or linear accelerator. The purpose of the linac is to generate protons at the ion source, accelerate these to a suitable level of energy, and drive them onto the *target.* The primary function of the target is to transform protons from the accelerator into neutrons. When high-energy protons bombard the target, some neutrons are knocked out, or "spalled", in a nuclear reaction called spallation [3]. To handle the 5MW proton beam power, the target station is equipped with powerful cooling systems. The target station contains components such as the tungsten target wheel and the target monolith. The monolith is composed of several thousand tons of steel, shielding the surroundings from radiation. When the target has generated neutrons, they are transported through apertures into the desired instruments [4]. A preliminary layout of the main components on the ESS site is shown in Figure 3.1.

KEY TO SYMBOLS

DETENTION PONDS	RECEPTION
LABS	ADMINISTRATION
NSS (INSTRUMENT HALL)	UTILITY BUILDING
TARGET	RADIOACTIVE MATERIAL HANDLING, STORAGE
ACCELERATOR HALL	EXTERNAL MEDIA
TRAM	TRANSFORMER SUPPLY BUILDINGS
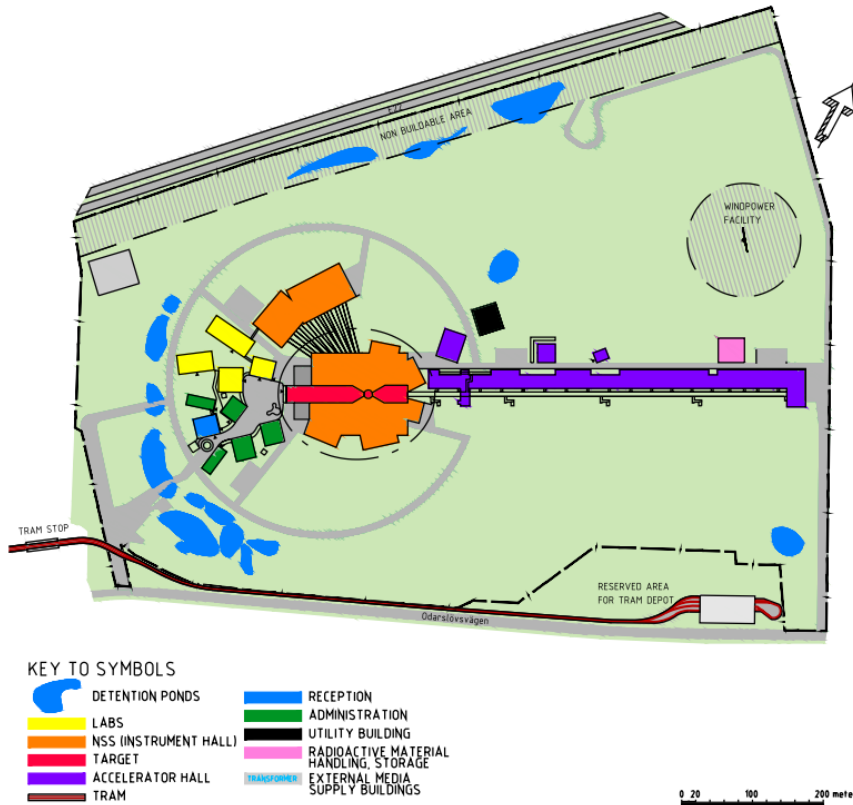
Figure 3.1. Preliminary layout of the main components on the ESS site. Image taken from [4].

To meet the need of the research areas, 22 instruments are currently being developed. Thus, different instrument classes such as powder diffraction and imaging have been defined. Depending on the instrument class, different energy spectra are needed to optimize performance [1, pp. 19, 21, 46]. Nearly all of the instruments will in one form or another be equipped with chopper systems [4, p.116].

The neutrons in the beam travel the same distance. However, they arrive at the neutron chopper at different times due to differences in energy, and thus velocity. A neutron chopper, also referred to as just chopper, is a type of pulse shaper, see Figure 3.2. A rotating disc is placed perpendicular to the beam to enable selection of neutrons with appropriate energy spectra depending on the scientific need. The chopper disc has one or more apertures, enabling neutrons arriving when the beam is aligned with the aperture to pass through. The other neutrons are absorbed by the chopper [5].
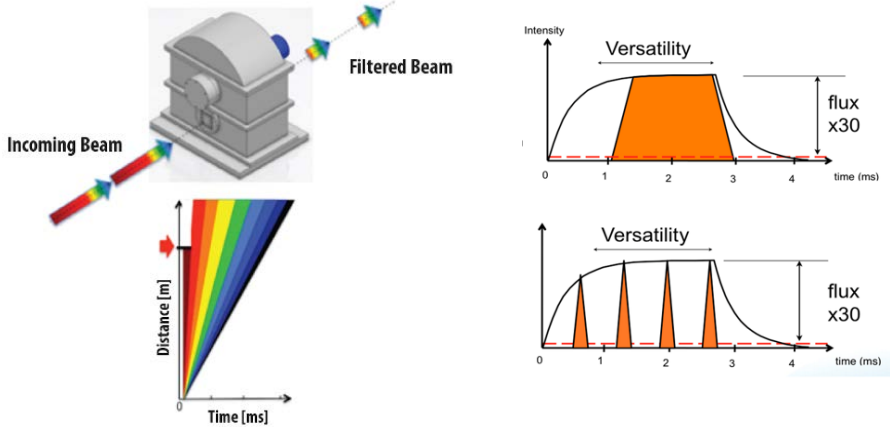
Figure 3.2. The neutron chopper filters out the required energy spectra. Image taken from [5] and [7].

During intermediate and slow rotational speeds of the disc, stresses are relatively low which allows for the disc to be made of a high strength aluminium alloy. This results in great flexibility of the disc design since this material is easily machined. At higher rotational speeds, superior mechanical properties are required which makes carbon fibre reinforced (CFR) discs a suitable option [4, p.120]. Carbon fibre reinforced plastics are frequently used in high performance applications due to properties such as high specific strength, high specific stiffness, and fatigue characteristics [6]. To protect the disc from radiation damage, it is coated with a boron carbide based absorber [7].

All chopper components must be designed to withstand the specified radiation exposure. The entire chopper system, see Figure 3.3, is designed to have a minimal lifetime of ten years. Furthermore, various components of the chopper system have a maintenance interval of at least five years. Since the disc has direct contact with the beam it is an *in-beam component.* Hence, the disc needs to withstand a high neutron dose of at least 200 MGy during ten years [8]. However, since the disc will be coated with a boron carbon-based absorber which will absorb some of the harmful neutrons,
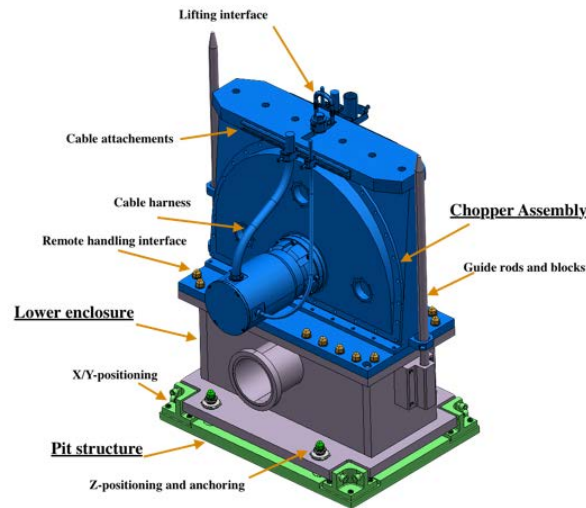
Figure 3.3. A 3D model of a neutron chopper system. Image taken from [8].

the CFRP will likely need to withstand a substantially lower dosage than 20 MGy per year.

3.2. Composites

A composite is a material with at least two distinct phases or constituents, termed *matrix* and *reinforcement.* Furthermore, the constituents must have different properties and they have to be present in reasonable proportions. The *matrix* is the component often present in the greater quantity. Composites may have a metallic, ceramic or polymeric matrix. The *reinforcement*, or *reinforcing phase* enhances the mechanical properties of the matrix. Thus, the reinforcement is generally stronger, stiffer and harder than the matrix. The dimensions and shape of the reinforcement affect its effectiveness, and thus determine the mechanical properties of the composite [9, pp. 3-5].

8

The reinforcement can be either *particulate,* i.e. in shape of particles, or *fibrous,* i.e. in shape of fibres. The former is approximately equiaxed, whilst the latter is characterized by a smaller cross-sectional dimension compared to its length. The fibrous reinforcement can be further categorized, depending on the ratio to cross-sectional dimension. If the ratio is high, the fibres are considered to be *continuous,* whereas fibres with a low ratio are referred to as *discontinuous* [9, pp. 3-5]. The different types of composites are illustrated in Figure 3.4.
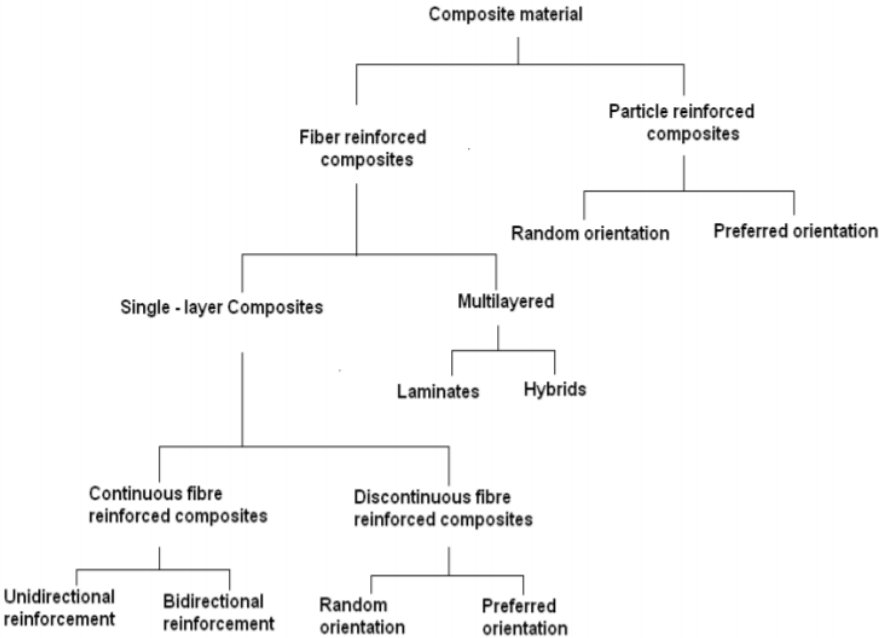
Figure 3.4. Different types of composites. Image taken from [9].

The orientation of the reinforcement affects the isotropy of the system. Discontinuous fibres can be oriented either randomly or preferred. In a continuous fibre composite, preferred orientation is frequently encountered and is referred to as *unidirectional.* The situation corresponding to the random orientation for discontinuous fibres is in the case for continuous fibres termed *bidirectional* woven reinforcement [9, pp. 3-5, 15].

Another category of fibre reinforced composites are *multi-layered* composites, which can be classified as *laminates* or *hybrids.* Laminates are made by stacking different layers, known as plies or laminae, in a certain sequence. Hybrids are composed of multilayers of mixed fibres [9, pp. 3-5].

Flexibility is important for fibres, since it determines if the fibres can be easily woven and thus impacts the choice of manufacturing method. Mainly, the flexibility of the fibre depends on the diameter D of the fibre and Young's modulus E_f;

$$\textit{Flexibility} \propto \frac{1}{E_f \times D^4} \tag{3.1}$$

Fibres with a large diameter and high Young's modulus are thus not flexible. Obviously, single fibres are not functional in structural applications due to their small cross-sectional dimensions. At the same time, entwining the fibres would not only restrict the dimension and shape of the components, but also introduce surface damage resulting in degradation in strength. To overcome these problems the fibres are embedded in the matrix to ensure protection of the fibre surface, separate the fibres, and distribute the load evenly throughout the reinforcement [9, p.12].

Resins made of thermosetting polymers cross-link during curing. The curing process is illustrated in Figure 3.5 and occurs during application of pressure and heat. Alternatively, a curing agent can be added which is a catalyst to facilitate the curing. The bonds in the cross-links are covalent just like in the polymer chain. These bonds restrict movement of the polymer chains, and thus the glass transition temperature will increase. Hence, the thermosets will become more brittle and will not be able to reshape during heating but rather degrade [9, p.169]. Heating epoxy may cause outgassing to occur, i.e. formation of bubbles in the epoxy. To avoid outgassing, it is important to wait until the infinite network of monomers has formed before heating the epoxy [10].
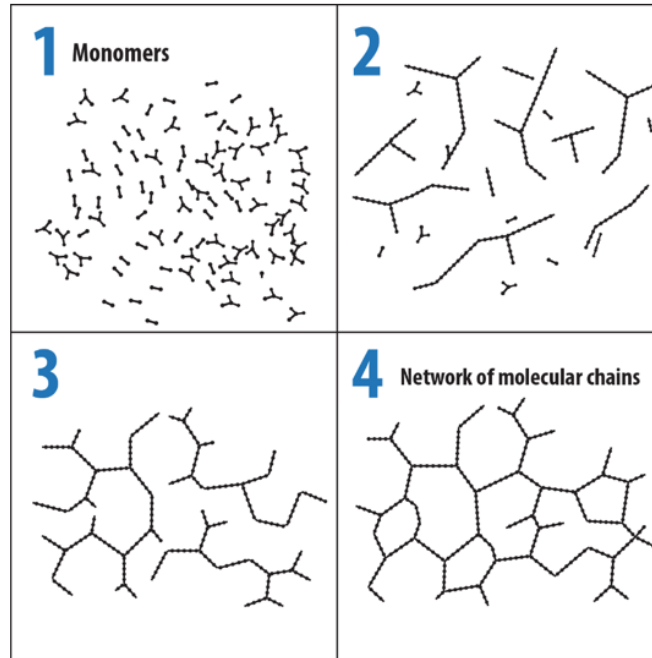
Figure 3.5. The different curing stages of epoxy.

Thermosets are often used as the resin since they often exist in a liquid state before the curing process, which allows for good impregnation of the fibres [6]. However, resins made of epoxy are relatively viscous which can result in difficulties impregnating woven fabrics [9, p.171].

3.2.1. Manufacturing Techniques

Generally, the volume fraction of the constituents is regarded as the most crucial parameter affecting the properties of the composite. A common problem during the manufacturing process is maintaining a uniform distribution of the reinforcement. The mechanical and physical properties are greatly affected by the homogeneity. Failure will initiate in the weakest part of the composite, and thus nonuniformity will affect the overall strength of the component. Hence, the ideal is to achieve a complete uniform composite [9, p.14].

The interface between the reinforcement and matrix have a big impact on the properties of the composite. If the stiffness and strength of the reinforcement are to be imparted to the composite, the reinforcements must be strongly bonded to the matrix. A strong interface results in high strength and stiffness, but a more brittle behaviour

and low fracture resistance. On the other hand, a weak interface produces a low strength and stiffness but high fracture resistance. Furthermore, the characteristics of the interface have an impact on other properties of the composite, such as resistance to fatigue, creep and environmental degradation. Clearly, the reinforcement and the matrix must be brought close together during the manufacturing process for interfacial bonding to occur. During some part of the process, the matrix is often in a state where it is capable of flowing. The extent to which a liquid will disperse over a solid surface is defined by the *wettability*. Good wettability implies that the liquid will cover every dip and bump of the surface of the reinforcement, displacing all air. When the matrix has wet the reinforcement bonding occurs [9, pp. 59-61].

The longitudinal strength of an aligned continuous fibre composite corresponds to the maximal strength of the fibre. As the angle between the fibre and the direction of the load increases, the strength decreases as shown in Figure 3.6. Thus, the lowest strength is reached when testing normal to the fibre direction and is referred to as transverse strength [9, pp. 94-95]. If the failure occurs at the interface, i.e. the two components get separated, it is known as an *adhesive* failure. However, if the failure occurs in the fibres or matrix it is referred to as a *cohesive* failure [9, p.65].
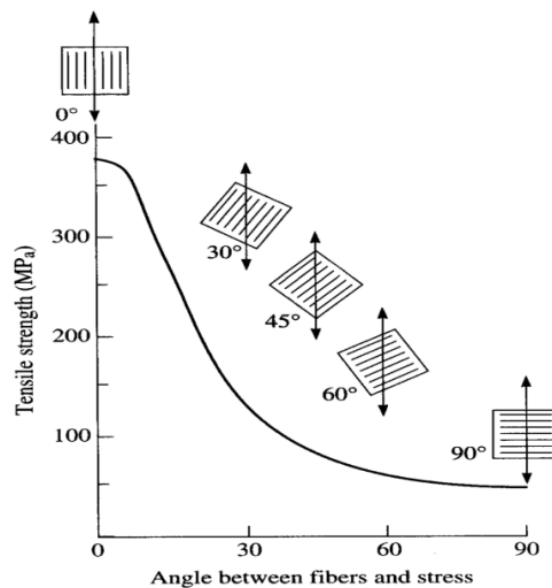
Figure 3.6. The link between fibre orientation and strength. Image taken from [10].

To achieve the desired strength and stiffness properties, unidirectional layers of different orientations are usually stacked together. These layers are often referred to as plies or laminae and are often cut from *prepreg* material and cured inside an autoclave or hot press. Prepreg is short for "pre-impregnated", where the matrix is already present bonding the fibres together. Laminates made from prepreg will normally contain between four and 40 layers, each ply with a thickness of around 0.125 mm [9, pp. 234-235]. There are a variety of well-established methods available for producing PMCs. Everything from simpler and labour-intensive methods to automated and rapid production methods. The choice of production method depends on several factors such as shape of component, number of components, required performance and cost [9, p.179]

3.2.1.1.   *Fabric Based Composites*

A commonly used alternative form of the polymer matrix composite is based on woven fibre reinforcement. Significant advantages in fabrication and handling are found in these PMCs compared to the conventional materials based on unidirectional prepreg. Furthermore, using woven composites can result in improved residual properties after impact and better containment of impact damage. However, using fabric reinforcement results in reduced laminate static strength and stiffness for two main reasons. Firstly, distortion of the fibres in the weave is inevitable. Secondly, fibre volume fractions in non-woven continuous fibre material, around 0.60 to 0.65, are generally not achievable in woven composites where the corresponding figure often ranges from 0.50 to 0.55. In addition, the stress concentrating effect of the fibre crossover points in the weave will result in sites for fatigue induced damage in the fibre-resin interface and the resin itself [9, pp. 384-385].

There are various weave patterns to choose from. Depending on the specific application, some patterns might be better suited than others, since various properties will be affected. Some of the basic weave types are plain, basket, and twill. They are illustrated in Figure 3.7.
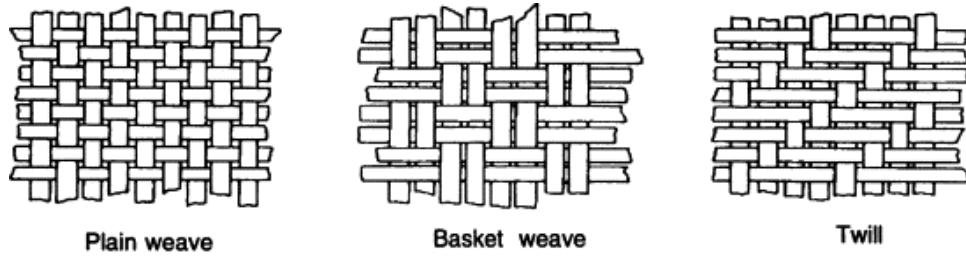
Figure 3.7. Common weave patterns. Image taken from [44].

A plain weave is shown in 3D in Figure 3.8.
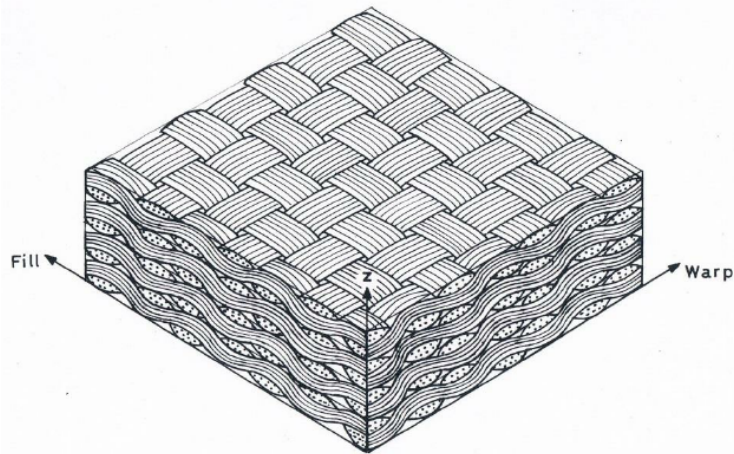
Figure 3.8. A plain weave shown in 3D. Image taken from [44].

3.2.1.2.   Manufacturing the Neutron Chopper Disc

The properties of the CFRP are strongly dependent on the manufacturing process. If some parameters are altered during the manufacturing, defects may occur causing high stress concentrations which can lead to laminate failure. Thus, manufacturing defects can cause serious degradation in terms of mechanical properties. Reducing or eliminating the defects occurring during manufacture is therefore crucial [6].

For spinning components, such as the chopper disc, it is important to manage interlaminar stresses. Hence, *polar woven fabric* is a good option since fibres are placed in both the radial and circular direction [11]. This results in sector rings, just similar to the plies, see Figure 3.9. Thereafter the weaving sector rings can be stacked into a disk [12]. Polar fabrics can also provide local reinforcement near flanges, holes, and

14

window frames on larger structures. In the case of utilization of expensive fibres for circular structures, the use of polar woven fabrics can minimize cutting waste and fabrication time [11].
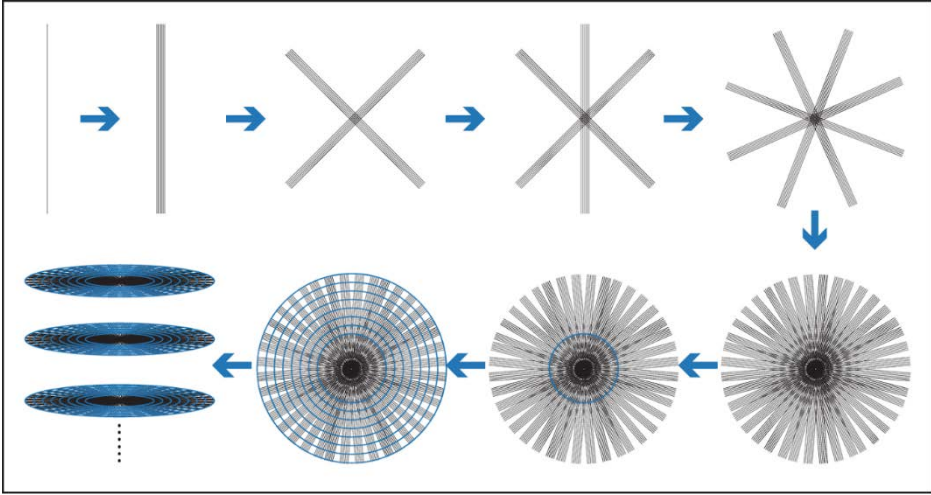
Figure 3.9. Illustration of the manufacturing process of polar woven fabrics.

3.3. Failure Mechanisms

Cracks in homogenous materials are less complex than those in composite materials. Some of the possible failure mechanisms for fibre reinforced composites are fibre fracture, fibre pull-out, matrix fracture, and debonding of the fibre-matrix interface. Usually one or more mechanisms are dominating the fracture behaviour. To understand how the fracture mechanisms work, it is important to comprehend the sequence of microscopic fracture incidents resulting in a macroscopic crack [13].
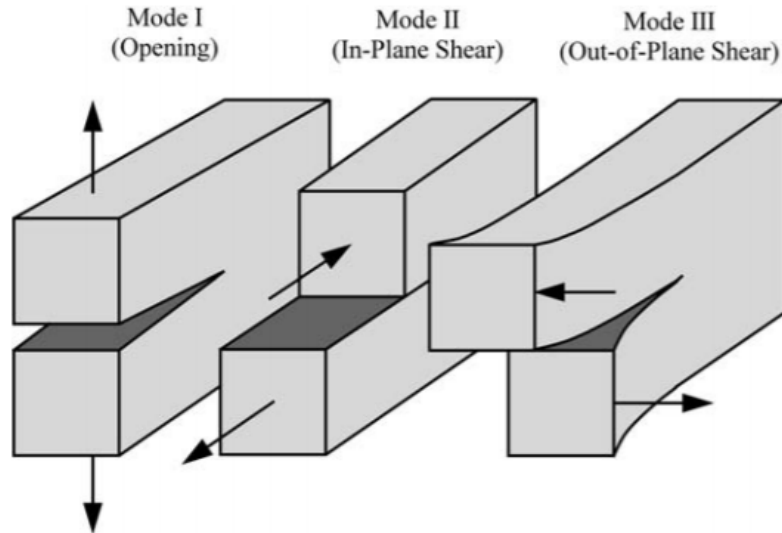
Figure 3.10. Macroscopic modes of cracks. Image taken from [9].

The crack can occur in different ways depending on the load, and thus it is described using different macroscopic modes, see Figure 3.10. In mode I, referred to as the opening mode, the crack faces are displaced normal to the crack plane resulting in opening of the crack. Mode II is termed shearing since one crack face tends to slide in relation to the other due to in-plane shear load. Mode III is out-of-plane shear loading, commonly known as tearing. Even when testing a composite material with simple geometry, the fracture can be complex. During a fracture test, all three crack modes can be operative [9, p.341].

The fracture process takes place in a small area near the crack edge, referred to as the process region. The process region is subjected to high loads, and material separations occur here. The physical appearance of the region and the physical process varies not only between different materials, but also due to environmental conditions such as loading rate and temperature. Significant processes occurring in the process region are nucleation and growth of micro-separation, eventually merging with the main crack. Micro-separation is a material separation, or decohesion, on a microstructural level. These micro-separations are nucleated at inhomogeneities in the material and depend on the load and material type. Examples of micro-separations are micro-cracks, voids, and disentangling of molecules. The micro-separations may be created by tensile or shearing forces, depending on the loading mode [14].

Three distinct phases are revealed during crack growth; loading without crack growth, stable crack growth, and unstable crack growth. During these loading phases, different regions evolve near the crack as can be seen in Figure 3.11. The region closest to the

crack edge is the process region, as previously mentioned. Outside the process region is the plastic region. When the crack edge advances, a wake of these two regions is left behind. In the wake of the plastic region, the material will deform elastically once again. Outside of these regions is the elastic region [13].
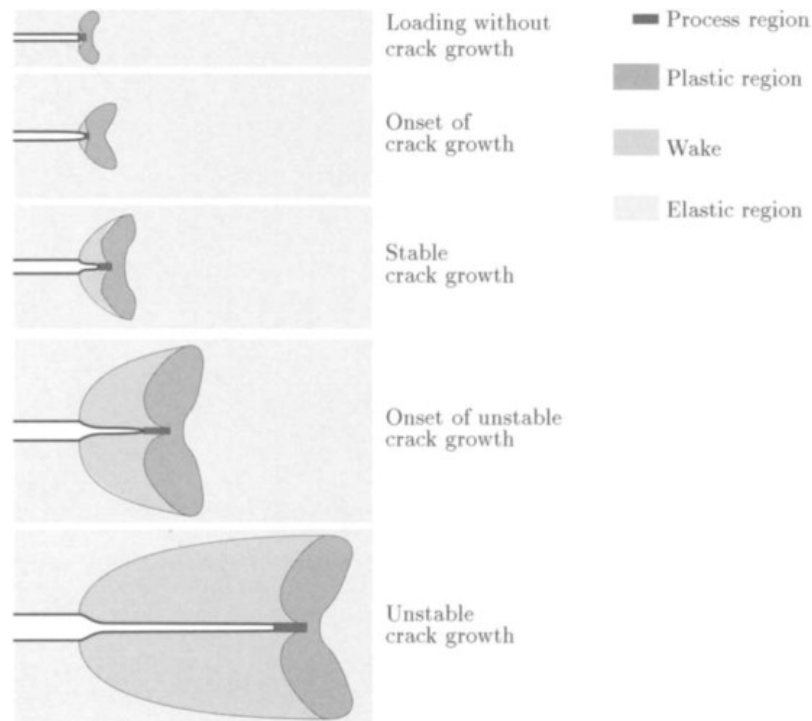
Figure 3.11. The phases of the fracture process and its corresponding regions. Image taken from [14].

In compression, the key phenomena are delamination and kink band formation [15], see Figure 3.12. The kink band is a result of micro-buckling of fibres, and thus the composite loses its load-bearing capacity [16]. In tension, the present phenomena are fibre rupture and pull-out also seen in Figure 3.12. When a crack begins to travel in the matrix approaching the fibres, it is stopped by the fibre. However, increasing the load increment may result in the crack passing around the fibre. Interfacial shearing of the fibres may induce further crack growth and debonding. Thus, fibres break at weak sites in the polymeric matrix. When the broken fibre end is pulled out of the grip of the polymer, total failure of the composite occurs. Microcracks and cracks in composites and polymers are generally hard to discover. Therefore, effective NDT, *non-destructive testing*, techniques are substantial to ensure that detection is not a limiting factor [13]. In bending, combinations of tension and compression occur [15].
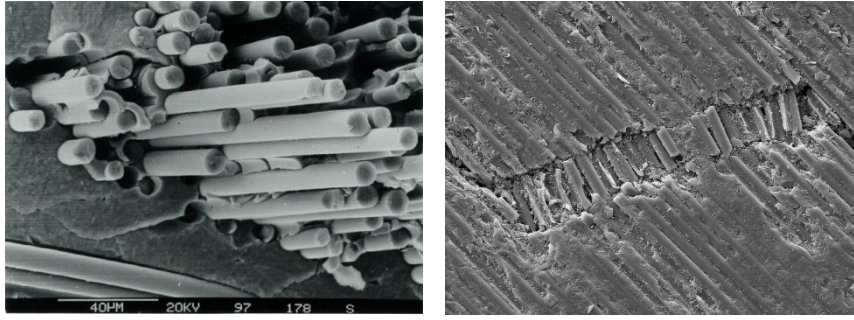
Figure 3.12. Illustrating fibre pull-out to the left and kink band formation to the left. Image taken from [45].

3.3.1. Toughening Mechanisms

One of the basic fracture-mechanic equations was established by Griffith. Griffith postulated the well-known concept that propagation of an existing crack occurs when reduction in potential energy is equal to or greater than the increase in surface energy due to creation of new surfaces. Classical linear elastic fracture mechanics, known as LEFM, is based on continuum mechanics. Furthermore, it assumes planar cracks with straight fronts, and the characteristics of the material structure are not considered. However, development of materials such as ultra-high strength steels, advanced ceramics and composites has shown that classical LEFM has limitations [17].

Due to some microstructural, environmental and local mechanical phenomena near the crack tip, the crack can experience what is known as crack tip shielding. This crack tip shielding, also referred to as extrinsic toughening, will affect the local near-tip "driving force". Extrinsic toughening involves mechanical modifications behind the crack tip, while intrinsic mechanisms are acting ahead of the crack tip. Selection of an appropriate curing agent, and other additives could intrinsically approve the crack retardation. Extrinsic toughness is related to processes and factors reducing the crack driving force. Some examples of these processes and factors are kinking, fibre bridging, and phase transformations. In a somewhat paradox way, extrinsic shielding mechanisms can also be a result of a network of small pores or cracks surrounding the crack front [17]. Some methods of crack retardation are shown in Figure 3.13.
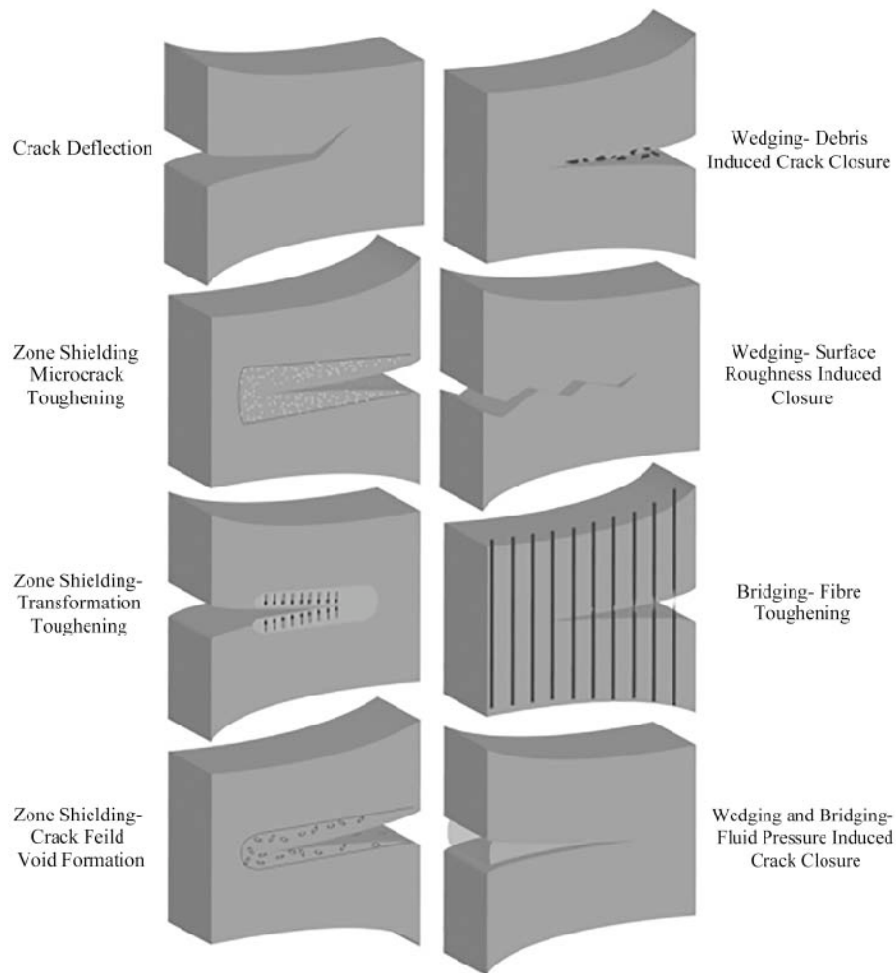
Figure 3.13. Crack toughening mechanisms. Image taken from [13].

More than one toughening mechanism is likely to operate although one mechanism may dominate. The effectiveness of the toughening mechanisms is dependent on several factors such as:

(i) volume fraction, size and morphology of the reinforcement

(ii) interfacial bond

(iii) properties of the reinforcement and matrix

(iv) phase transformations

Considering these parameters, it is not surprising that the dominant mechanism varies for different composites. For some composites it is difficult to determine the dominant mechanism, due to the complexity of the situation [9, pp. 342-343].

During debonding, new surfaces in the composite are created and thus requires energy. Since the total area of the created surface can be large, the total required surface energy

is significant. To maximize the toughening due to debonding, a large volume fraction of fibres is required. Furthermore, the fibre-matrix interface is weak while the fibres themselves are strong. Without debonding, fibre pull-out would not occur. As normal friction forces must be overcome, a force is required to pull out the fibre. In addition, the fibre has relaxed after the debonding, resulting in expansion and thus jamming of the fibre in the matrix [9, pp. 342-349].

3.4. The Presence of Radiation at ESS

To understand how radiation affects the material, it is crucial to first understand what radiation is, why and where it occurs. As previously mentioned, the target transforms the proton beam from the linac into fast neutrons as the useful product, via the spallation process. However, a large amount of heat and radiation are generated as inescapable by-products. The spallation material for this neutron production is tungsten, since it is known to yield the highest number of neutrons per incoming proton. The target is surrounded by a *moderator* which transforms the fast neutrons emitted by the target into slow neutrons. Fast neutrons refer to velocities in the range of 10% of the velocity of light, while the velocities of slow neutrons are comparable to the speed of sound [4, pp. 149-172].

Apart from spallation, neutrons can also be produced using a fission reactor. During fission the nucleus splits into two parts and some neutrons due to the high energy level. The high energy is related to the compound nucleus that forms when the incident neutron enters the heavy target nucleus. Since the compound nucleus temporarily contains all the mass and charge, it exists in an excited state. The additional excitation energy equals the particle's kinetic energy plus the contribution of binding energy. This excitation energy may cause oscillations, distorting the compound nucleus. The oscillation may lead to the compound nucleus becoming dumbbell-shaped. Nuclear fission occurs when the repulsive electrostatic forces exceed the attractive nuclear forces. Thus, the excitation energy must be above the *critical energy* for fission to occur. A large amount of energy is then released as kinetic energy and radiation [18].

Neutrons produced from the fission process have an average energy level of 2 MeV. However, they begin to slow down immediately due to the numerous scattering

reactions. After these collisions with nuclei, the speed of the neutron almost equals the kinetic energy of the medium atoms. Since this energy is temperature-dependent, it is commonly referred to as *thermal energy*. Furthermore, *thermal neutrons* refer to neutrons with energies in the region < 1 eV. The moderator should not absorb the neutrons, but rather slow down the speed during few collisions. A small number of collisions is preferable to avoid excessive neutron leakage [18]. A spallation source does not create the reactivity threat posed by a fission reactor, and it does not have the same level of decay heat generated from a fission process [4, p.600].

The more neutrons produced during the spallation process, the "brighter" is the neutron source considered to be. ESS will be around 100 times brighter than existing spallation sources [19]. The flux at ESS will be 30 times higher than the world's most powerful reactor-based neutron source. In addition, ESS will offer five times more power than any other accelerator-based spallation source [4, p.5].

3.4.1. Radioactive Decay

In their naturally occurring state, heavy elements such as uranium and its decay chain elements emit radiation. Emitting radiation is a spontaneous disintegration process also known as *nuclear decay* or *radioactive decay*. Alpha decay is the emission of alpha particles which are identical to the nucleus of a helium-4 atom. The alpha particle has a charge of $+2$ since it does not have any electrons. This positive charge enables the alpha particle to remove electrons from the orbits of atoms in its vicinity. Removal of electrons requires energy and thus the energy of the alpha particle reduces for each reaction. Due to its large mass and strong positive charge, the alpha particle deposits a lot of energy during a short distance of travel. Thus, the penetration of alpha particles is limited. Most alpha particles are stopped by a sheet of paper [18].

Beta decay is the emission of a high speed, high energy electron expelled by the atomic nucleus. Collisions with orbiting electrons result in *ionization*. The beta particle is slowed down after every collision due to reduction of kinetic energy. When the beta particle is slowed down further, it will eventually be captured as an orbiting electron in an atom. Beta radiation is more penetrating than alpha, but can be stopped by a few millimetres of metal [18].

Gamma emission is a high-energy electromagnetic radiation originating in the nucleus. It is emitted in the form of photons that have both particle and wave properties. Since gamma ray has no charge and no mass it is hard to stop and is thus very penetrating. A small fraction of the original gamma will go through several decimetres of concrete [18].

The penetration levels of alpha, beta and gamma decay are illustrated in Figure 3.14.
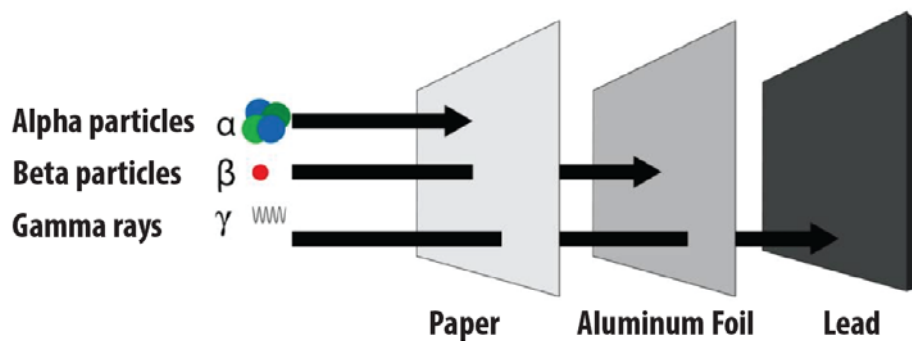
Figure 3.14. Penetration level of alpha, beta and gamma decay.

Radiation is measured in terms of absorbed energy per unit mass of tissue and is referred to as *Gray* or *Gy*. One Gray equals one joule per kilogram, also known as 100 rad [20].

3.4.2. Radiation Damage

Different radiation effects can be divided into the four following categories:

1. Impurity Production

   Impurity production refers to impurities caused by radiation and not potential impurities that pre-exist in the material. The impurity production happens when nuclei transmute into other nuclei, like hydrogen or helium. This may cause swelling in the material due to the pressure exerted on its surrounding atoms. Thus, the mechanical and electrical properties can be affected [21].

2. Atom Displacement

When an energetic particle is scattered by an atomic nucleus, the kinetic energy transferred in the collision will be enough to break the chemical bonds to the surrounding atoms [22]. The first atom to be ejected from its normal lattice position is known as a *primary knock-on* and may serve as a projectile to produce further displacements. Defects such as interstitials, vacancies, and dislocations are thus created [21].

3. Ionization

During ionization, interaction with the electrons surrounding a neutral atom occurs. Removing electrons creates charged ions which affect the bonding of the materials. For covalent bonds, where atoms are held together by sharing of electrons, ionization causes a lot of damage. Furthermore, the chemical composition of the material is changed. Organic compounds such as plastics are almost only made up of covalent bonds. For ionic bonds, ionization is not as destructive. Since metallic bonding consist of a sea of electrons, the removed electrons by ionizing radiation will quickly be replaced due to the free movement of electrons. Metallic bonds are thus least affected whilst covalent bonds are affected the most [21].

4. Large Energy Release

Due to radiation, energy deposition within the material occurs. In organic compounds, this energy breaks chemical bonds. In metals it appears as heat [21].

3.4.2.1.   *Effect of Radiation on Polymers*

Due to the altering of the chemical bonds, plastics are greatly affected by radiation. However, not all polymers are affected the same way. Generally, irradiated polymers undergo fracture of polymer molecules known as *chain scission*, and cross linking. Both reactions alter the properties of the polymer. For example, chain scission decreases the molecular weight while cross linking increases it [22].

Furthermore, chain scission generally decreases Young's modulus, increases elongation, decreases hardness and reduces yield stress. It may lead to embrittlement and release of gas, and thus it may increase the thermal conductivity. In general, cross linking hinders the viscous flow, increases hardness, decreases elongation, increases Young's modulus, and causes embrittlement [22]. Chain scission can supersede crosslinking and vice versa resulting in a nonlinear or oscillatory variation in the Young's modulus [23].

3.5. Previous Studies

Currently, there is limited knowledge of how high doses of radiation affects CFRP. A study performed by Hoffman and Skidmore evaluated the gamma radiation resistance for a composite made of carbon fibres woven into a plain weave cloth, and epoxy. The composite was exposed to three different gamma doses; 0.5, 1.0, and 2.0 MGy. The structural changes as well as the tensile strength and hardness were examined. Furthermore, differential scanning calorimetry (DSC) was used to examine the epoxy resins from the baseline and 2.0 MGy bars to identify possible modes of degradation and thermal transitions. However, testing of the epoxy matrix only revealed changes in thermal properties, spectroscopy result, and hardness with an increased gamma radiation [24].

A load cell with a capacity of 88 900 N was used, with a crosshead speed of 0.127 cm/min. Three baseline bars and six irradiated bars were tested until failure by fracture. Mechanical testing of the specimens showed no apparent change in strain to failure, fracture strength, or modulus after exposures. The fractures of the unirradiated specimens were nominally perpendicular to the length of the specimen. The damage due to fracture was primarily limited to the fracture area. Protruding fibres were discovered at the fracture surface, but minimal delamination was seen outside the fracture area. The fractures of the bars exposed to 0.5 MGy and 1.0 MGy looked approximately the same as the unirradiated ones. At the highest dose of 2.0 MGy, damage extends several centimetres along the length of the specimen and is not limited to the fracture site. In addition, pockets of resin are absent at the interface between carbon fibre woven points. A noticeable volume of resin was also missing from the interior of the specimen [24].

Scanning electron microscope, SEM, was then used to examine the fracture surfaces more closely and identify any fracture mode or microstructural changes after gamma irradiation. Fibre pull-out containing minimal polymer debris was observed in the baseline samples, suggesting failure at the interface between the epoxy and fibres. The dimpled fracture surface of the epoxy matrix demonstrates a ductile fracture [24], see Figure 3.15.
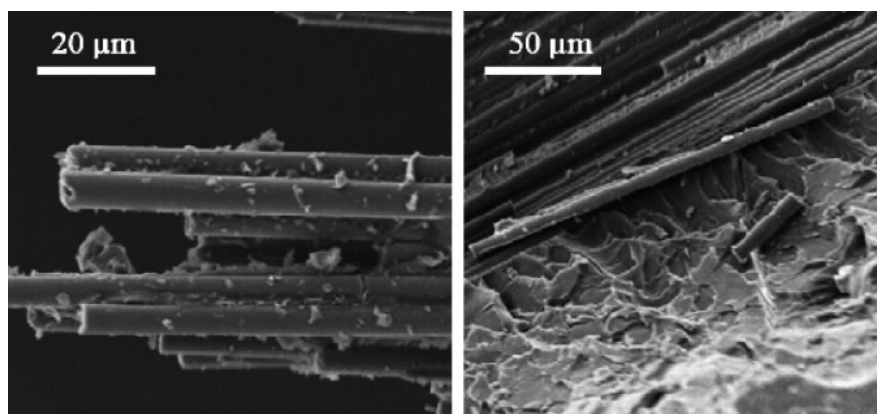
Figure 3.15. Unirradiated sample showing minimal polymer debris on the fibres and a dimpled fracture surface of the epoxy, indicating a ductile fracture. Image taken from [24].

For the 0.5 MGy irradiated specimens, minimal debris on the fibres once again suggest interfacial failure as the main failure mechanism. However, the facets on the fracture surfaces of the epoxy indicate a more brittle fracture [24], see Figure 3.16.
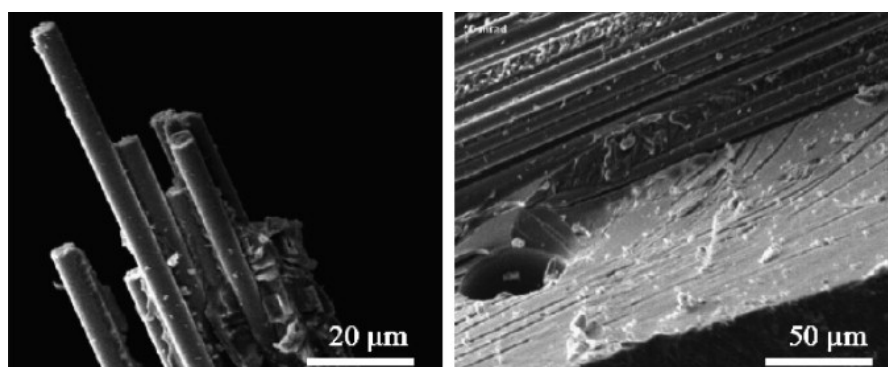
Figure 3.16. Specimen subjected to 0.5 MGy gamma radiation with small amount of resin debris on the fibres and a fracture surface indicating a lower degree of ductility than the unirradated sample. Image taken from [24].

The samples exposed to 1.0 MGy had significant amount of polymer debris attached to the carbon fibres. Thus, the primary failure mechanism is fracture through the epoxy

rather than along the interface between the epoxy and carbon fibres. Furthermore, the fracture surface indicates an even more brittle fracture than before [24], see Figure 3.17.
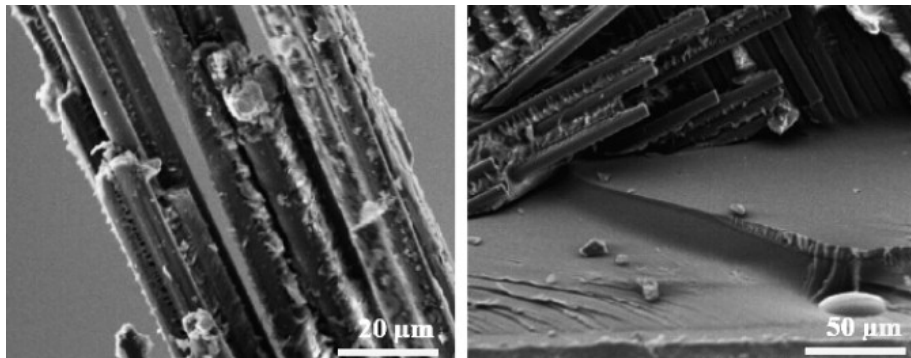
Figure 3.17. Sample irradiated with 1 MGy showing significant amount of resin attached to the fibre and a fracture surface indicating a more brittle fracture. Image taken from [24].

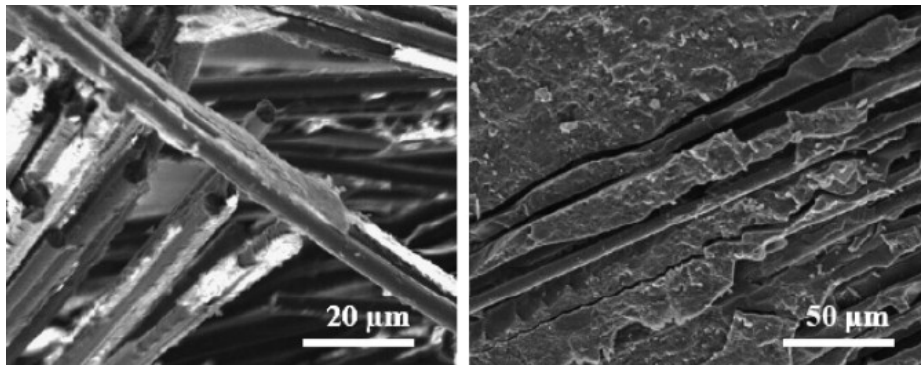For the specimens exposed to 2.0 MGy, significant polymer debris is found on the carbon fibres and several cracks run through the epoxy [24], see Figure 3.18.

Figure 3.18. Sample irradiated with 2 MGy showing a lot of resin attached to the pulled-out fibres and several cracks through the epoxy. Image taken from [24].

Further evidence of degradation was observed in the specimens irradiated at 2.0 MGy which had several bulges covered in cracks. These may be the result of the release of gas from the epoxy upon post-curing or a radiation decomposition phenomenon. Moreover, the DSC showed a slight increase in glass transition temperature which in combination with the mechanical test results and SEM images point towards resin degradation [24].

3.6. Analysing Microstructural Damage

To analyse potential microstructural damage within the material it is crucial to look inside of it. Two techniques that can be used to do this are with the use of X-rays and neutrons. When using the former technique, X-rays are diffracted by the material and thus the relative atomic positions can be figured out. However, this technique is dependent on electrons surrounding the nucleus of the atom since the X-rays are scattered by these. Thus, light atoms with few electrons do not scatter X-rays efficiently compared to heavy atoms [25].

Neutrons have no charge and are therefore much more desirable than charged particles when it comes to penetrating matter, see Figure 3.19. Moreover, the size of a nucleus is around 100 000 times smaller than the distance between two nuclei. Therefore, neutrons do not have a high risk of being absorbed or scattered and can thus travel large distances through most materials [25]. The effective area of the nucleus presented to the passing neutron is called the *total cross section* σ_T. The cross section is measured in barns (1 barn = 10^{-24} square centimetre) and describes the interaction of a neutron and a single nucleus. It will either interact through absorption or scattering. The cross section for absorption σ_a represents the probability of a neutron being absorbed by a specific atom. The cross section for scattering σ_s represents the probability of a neutron being scattered of a particular nucleus [18]. If the cross section is hit by the neutron, it is scattered isotropically [25]. Thus, the total cross section equals the sum of cross section for scattering and the cross section for absorption [18].

$$\sigma_T = \sigma_s + \sigma_a \tag{3.2}$$

Except for neutrons and X-rays, electrons can be used to look at the microscopic structure of materials. Electrons interact with the material electrostatically and do not penetrate matter very deeply, see Figure 3.19. However, to fully understand the structure of a material, electron microscopy is frequently used [25].
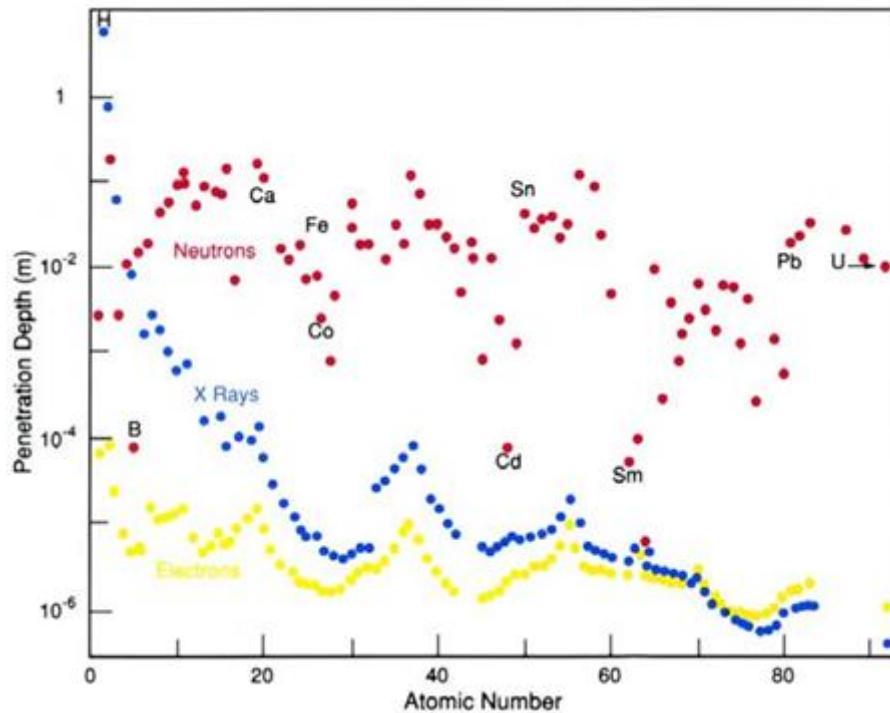
Figure 3.19. Penetration depth to atomic number for X-rays, neutrons and electrons. Image taken from [25].

To summarize, X-rays interact with electrons while neutrons interact with the nucleus of the atom. Since the interactions differ, complementary use of neutrons and X-rays in imaging will provide additional information. Furthermore, electron microscopy is frequently used to provide additional information on the structure [26].

3.6.1. Tomography

To receive information about the structure of the inside of an object without affecting the sample integrity or disassemble the structure, NDT methods are required. A common NDT method is computed tomography which uses projection images from several views to reconstruct the structure inside the sample, see Figure 3.19. This method can be performed using both neutrons and X-rays. The sample is placed on a turntable which enables rotation in equiangular steps over 360 or 180 degrees to cover the sample and thus obtain the desired projections. A scintillator is used to convert neutrons into visible light which can be registered by a CCD-camera and ejected as projection images. Special reconstruction software is then used to reconstruct the sample.
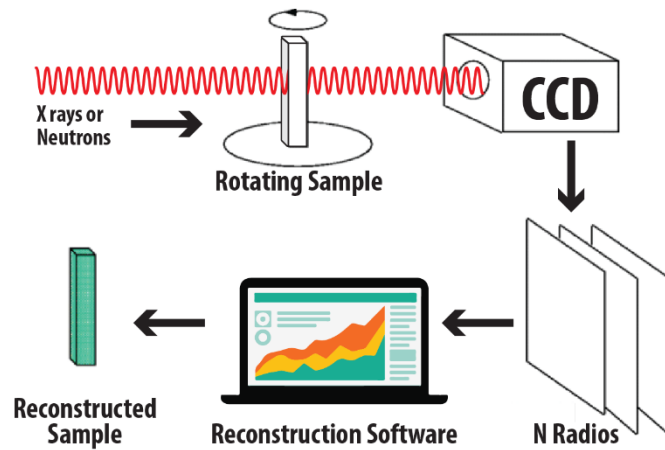
Figure 3.20. The principle of tomography.

The reconstructed sample can then be used to create sliced images perpendicular to the rotation axis [27, pp. 6,22], see Figure 3.20.
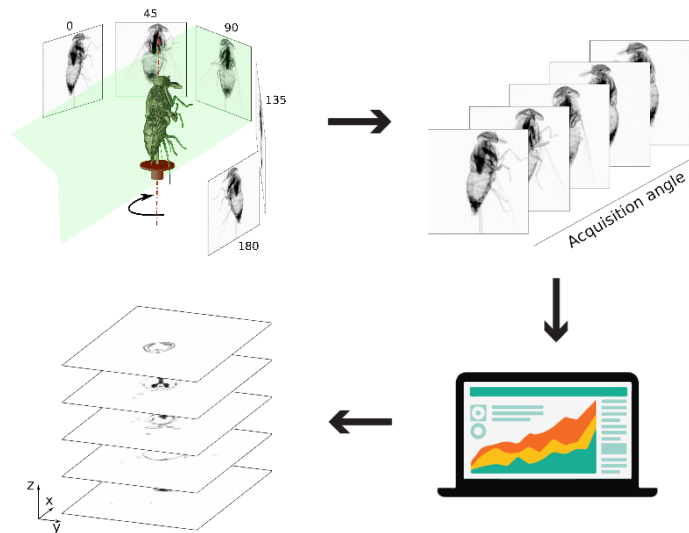
Figure 3.21. Illustrating the process of creating perpendicular image slices. Image recreated using [27].

3.6.2. X-ray Imaging

X-ray tomography is usually performed by using a synchrotron or laboratory X-ray source. One of the major differences between the sources is that the synchrotron source produces parallel X-ray beams, while the laboratory source produces a cone beam using a tube, see Figure 3.21. This is also the reason why the sample often requires to be rotated 360 degrees when using the laboratory source, whilst 180 degrees often is sufficient enough for the synchrotron source [28].
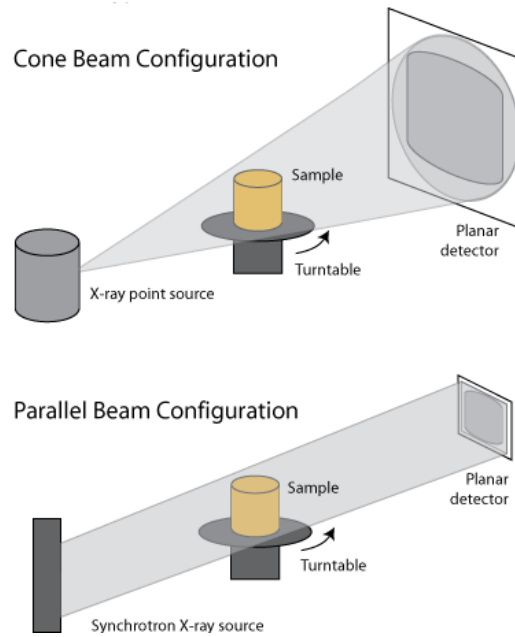
Figure 3.22. Cone shape beam at the top, and parallel beam at the bottom. Image taken from [30].

3.6.2.1.   *Laboratory X-rays*

The X-ray source can be operated at voltages ranging from 30 kV to 160 kV. A thin transmission target made of tungsten is hit by electrons produced by thermionic emission. As a result, an electron from one of the shells around the atomic nucleus is ejected. Hence, the atom is highly unstable which leads to an electron repositioning itself from a higher to a lower energy level, releasing energy in the form of X-rays.

The cone beam is delivered with a focal spot that can be altered in size. Reducing the focus size results in an increased resolution due to reduction of the geometrical blurring effect, see Figure 3.22. However, a reduced focal spot also reduces the flux of X-rays and thus requires a longer exposure time [28].
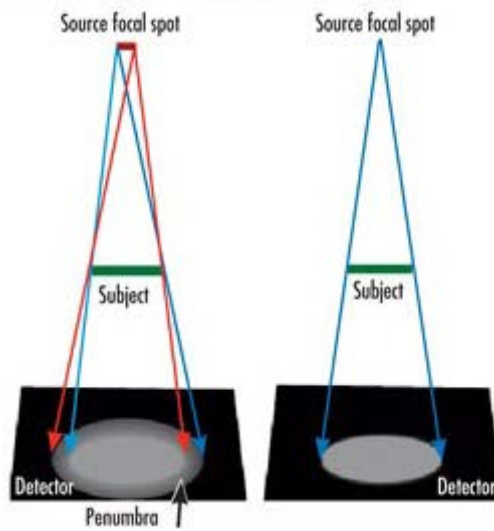
**Figure 3.23. Influence of focal spot size.
Image taken from [28].**

3.6.3. Fundamental Principles of Imaging

The proportions of absorbed or scattered beams passing through the material are reflected by the attenuation and illustrated as grey levels in each slice as each voxel is passed through. Thus, tomographic imaging is based on measuring the decrease in beam intensity along a number of linear paths [29, 30].

The attenuation of a monoenergetic beam penetrating a homogenous material is described by Beer-Lambert's law:

$$I = I_0 \exp[-\mu x] \tag{3.3}$$

where I is the detected intensity, I_0 is the initial beam intensity μ is the linear attenuation coefficient for the examined material, x is the distance of the beam path through the material. However, if the object is composed of several materials the equation becomes

$$I = I_0 \exp\left[\sum_i (-\mu_i x_i)\right] \tag{3.4}$$

where i represents each material with path length x_i and attenuation coefficient μ_i. Since both the neutron and X-ray beam are *polychromatic*, the attenuation coefficients are written as a function of the beam energy E [29, 30]. Hence, the equation becomes:

$$I = \int I_0(E) \exp\left[\sum_i (-\mu_i(E)x_i)\right] dE \tag{3.5}$$

3.6.4. Imaging Artifacts

Due to production methods laboratory X-rays are as previously mentioned polychromatic, which give rise to beam hardening. Beam hardening is a result of arresting of the softer X-rays during entering of an attenuating specimen [28]. Materials with high atomic number have a much greater attenuation effect at lower energies. Attenuation of X-rays is primary due to photoelectric absorption for low energy X-rays, and due to Compton scatter for high energies. The dark streaks are the result of both scattering and beam hardening since they cause more photons to be detected than expected. Using a higher energy, results in less beam hardening artefacts due to a harder X-ray beam. However, at higher energy levels the contrast is hard to achieve [31]. Although it is possible to filter out the soft X-rays, this results in longer scanning times [28].

Another common artifact is the ring artifact which can be seen as partial or full circles centred at the axis of rotation. This is caused by an overlap of X-rays with abnormal values due to a shift in the output from one or several detectors. The shift can be caused by many factors, such as a change in temperature or beam energy. However, these can be controlled by calibration of the detector and regulation of the experimental conditions [32].

Synchrotron sources generate a monochromatic beam due to high proton flux, and thus will not generate beam hardening [28]. Beam hardening produces dark streaks between dense objects, and bright streaks can often be seen adjacent to these [31].

With the same reasoning, the previously mentioned artifacts can occur during neutron imaging as well. It is important to correct these distortions before reconstruction, since

the reconstruction process will amplify noise. To obtain even more constant pictures, an empty image can be used as a reference to show how much correction is necessary for each pixel on every projection [33].

For each pixel i of all P_ϑ projections;

$$R_\vartheta(i) = P_\vartheta(i) \times \frac{1}{P_{empty}(i)} \tag{3.6}$$

where R is the homogeneity corrected image, and P_{empty} is the empty image.

3.6.5. Scanning Electron Microscope

By using scanning electron microscopy (SEM), it is possible to get images of higher performance compared to light microscopy. SEM offers larger depth of field and higher resolution, which makes it possible to see very small features. Furthermore, features of different heights can be in focus. The SEM scans a sample using a focused beam of electrons and thereby generates an image. The main components of an SEM are:

- Source of electrons
- Vertical column which electrons travel using electromagnetic lenses
- Electron detector
- Sample chamber
- Computer and display to view the images

The electron gun is the source of electrons and is placed in the top region of the microscope. To attract the electrons away from the filament in the electron gun, an anode is placed below. A primary beam of electrons is thereby directed towards a sample at the bottom of the SEM. The sample will thereafter give off different types of electrons collected by different detectors, see Figure 3.26.
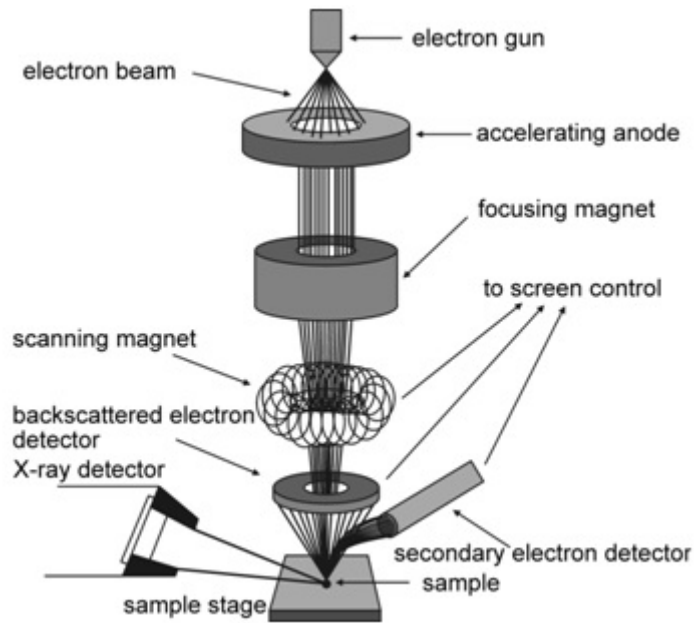
Figure 3.24. Schematic illustration of an SEM. Image taken from [34].

Electrons from the primary beam interact with the sample in two different ways, see Figure 3.27. The first is by replacing electrons of sample atoms, generating secondary electrons. These electrons generally have very low energy and therefore only escape from the surface of the sample, generating an image with contrasts based on the topography of the sample. More electrons are generated from peaks compared to valleys. Hence, the valleys are dark, and the peaks are bright.

The second way in which the primary beam interacts with the sample is by generating backscattered electrons. These are electrons which directly come from the primary beam. Backscattered electrons therefore have higher energy. Atoms with a higher atomic number will backscatter more electrons and look brighter. By scanning the sample surface in a rectangular pattern, the beam creates a variation in signal strength moving from point to point. The strength of the signal reflects the differences in the sample. A virtual image is then constructed based on the output signal [34].
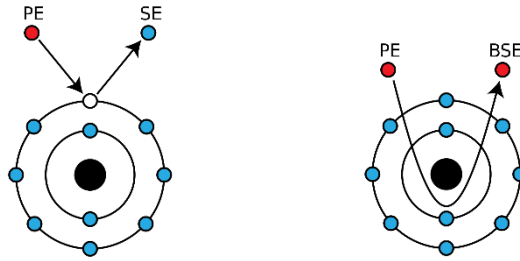
Figure 3.25. Secondary and backscattered electrons.

When non-conductive specimens are scanned by the electron beam, they collect charge. This can cause image artifacts and other scanning faults. To prevent these scanning faults, non-conductive materials are usually coated with an electrically conducting material [35].

3.7. Analysing Macroscopic Damage: Three-point Bending Test

The three-point bending test is extensively used in material characterization due to several reasons. Simplicity of sample preparation and testing, suitability for fatigue testing and cyclic loading, and convenience for studying fracture toughness are some of those reasons. However, one of the main reasons to use three-point bending is because the specimen is subjected to compression, tension, and shear simultaneously. Hence, the three-point bending test is a good way of measuring the structural integrity of the material [36]. Furthermore, three-point bending is suitable for a range of materials, including thermosetting materials with reinforcement [37]. The principle of three-point bending is illustrated in Figure 3.23.
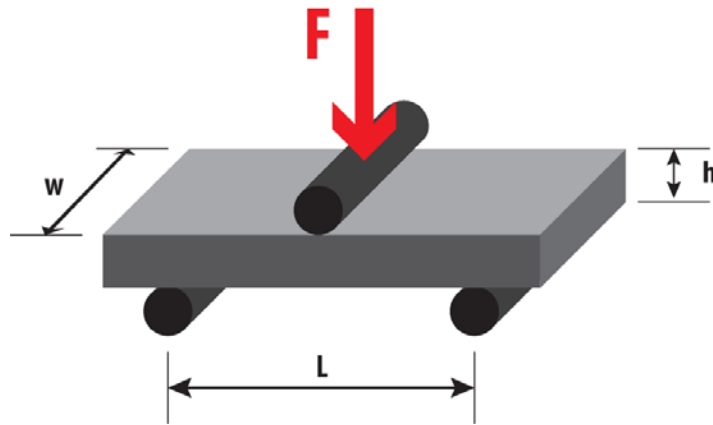

Figure 3.26. The principle of three-point bending.

The stress and strain are calculated as shown in (3.8) and (3.9), respectively.

$$\sigma_f = \frac{3FL}{2wh^2} \tag{3.7}$$

$$\varepsilon_f = \frac{6sh}{L^2} \tag{3.8}$$

σ_f is the flexural-stress parameter

F   is the applied force, in newtons

L   is the span, in millimetres

w   is the width, in millimetres, of the specimen

h   is the thickness, in millimetres, of the specimen

ε_f is the flexural strain parameter in question, expressed as a dimensionless ratio or as a percentage

s   is the deflection, in millimetres

v   is the test speed, in millimetres per minute

r   is the flexural strain rate, in percent per minute

Typical stress strain curves are shown in Figure 3.24. As can be seen in the figure, the flexural stress at break is denoted σ_{fB}, while the maximum stress is denoted σ_{fM}. The corresponding flexural strain is ε_{fB} at break, and ε_{fM} at the maximum stress level.
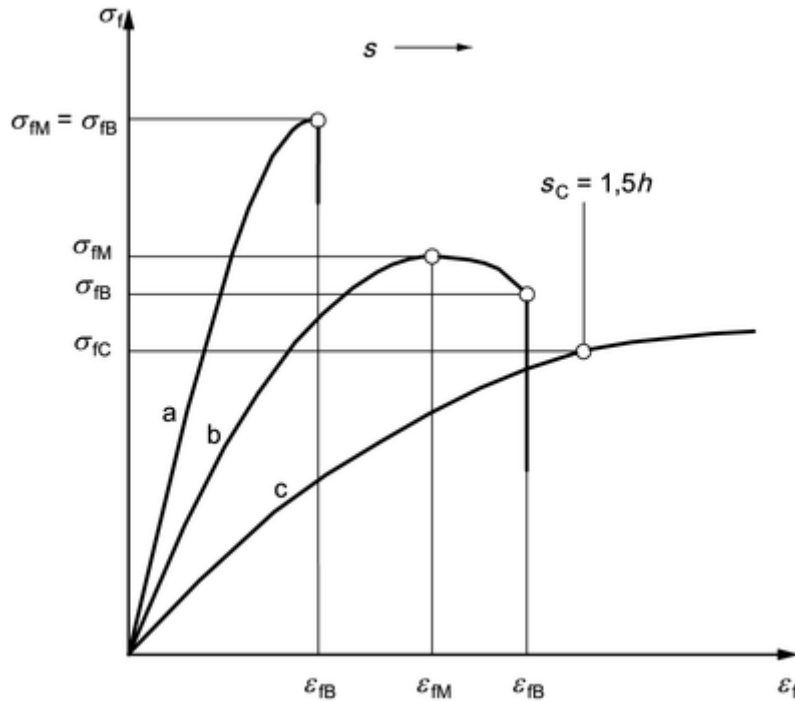
Figure 3.27. Typical stress-strain curves from three-point bending.
Image taken from [37].

If a small load is not applied prior to testing, a curved region at the beginning of the stress-strain diagram may occur.

$$v = \frac{rL^2}{600h} \tag{3.9}$$

For modulus determination, the test speed should be set in accordance with the standard for the material being tested. In the absence of this information, a value that

37

gives a flexural-strain rate as near as possible to 1 %/min should be selected. The three-point bending test machine is shown in Figure 3.25.

Figure 3.28. The three-point bending machine.

The standard specifies the distance between the supports to:

$$L = (16 \pm 1)h \tag{3.10}$$

4. Neutron Chopper Disc Test Specimen Description and Radiation Process

Two different composites are compared in this study. Both composites are made of epoxy and woven carbon fibre, manufactured by the organisation *Airbus.* The stacking sequence of the weave is the same for both composites, a lay-up of [0/90/0/90]s twill weave is used as shown in Figure 4.1 [38]. However, the compositions of the epoxies are slightly different, see Figure 4.2. Thus, manufacturing parameters are also affected.
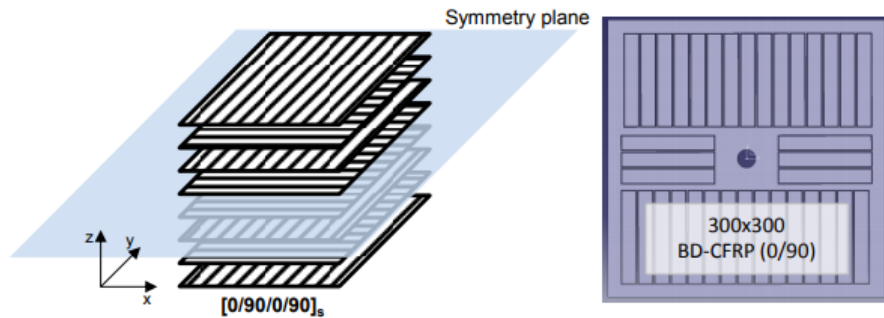
Figure 4.1. Illustration of the sample manufacturing. Image taken from [38].

After production, the samples are cut out. The thickness of the plates does not deviate more than ±5 %. Due to some manufacturing limitations, different parts of the batches were used, i.e. not all the samples from each type were milled out from the same position [38].

The two different composites are referred to as *type A* and *type B.* The neutron cross section of each element is presented in Table 4.1 [39].

A-Composite (60% FVC)						
FVC	60%					
Element	C	H	O	Cl	N	S
Total [g/mol]	95,7	10,8	16,1	7,4	16,6	0,5

B-Composite (60% FVC)						
FVC	60%					
Element	C	H	O	Cl	N	S
Total [g/mol]	91,1	8,2	19,9	7,5	8,3	0,5

Figure 4.2. Composition of the resins in type A and B.

Table 4.1. Neutron cross section of each element in the resins.

Element	Neutron absorption cross section σ_a
C	0.0035
H	0.3326
O	0.00019
Cl	33.5
N	1.9
S	0.53

The samples were then irradiated using the IBR-2 reactor in Dubna, Russia with radiation doses of 3, 10, and 30 MGy. Figure 4.3 illustrates the irradiation process. Figure 4.4, Figure 4.5 and Figure 4.6 illustrate the types of neutron energy spectra that hit the samples. They also illustrate the flux of these neutrons in relation to the distance from the moderator. Furthermore, some samples of each type were kept unirradiated for reference.
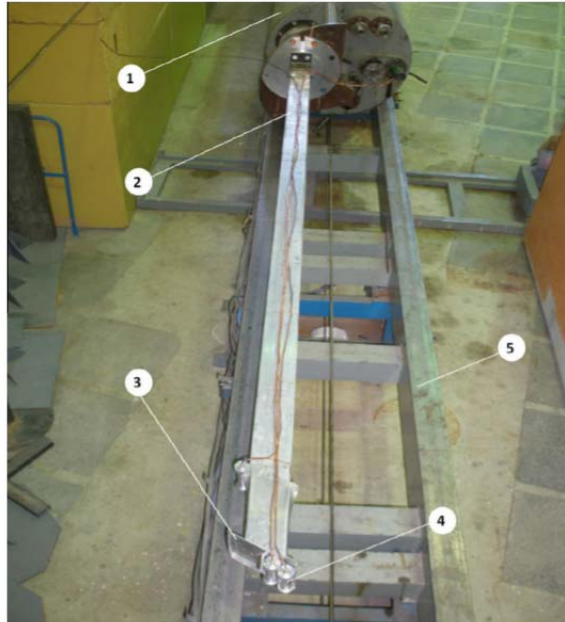
Figure 4.3. The irradiation facility at IBR-2 reactor experimental hall, the view from the external biological shield side: 1 – massive part of the irradiation facility, 2 – transport beam, 3 – metallic container for samples fastening, 4 – samples, 5 – rail way.
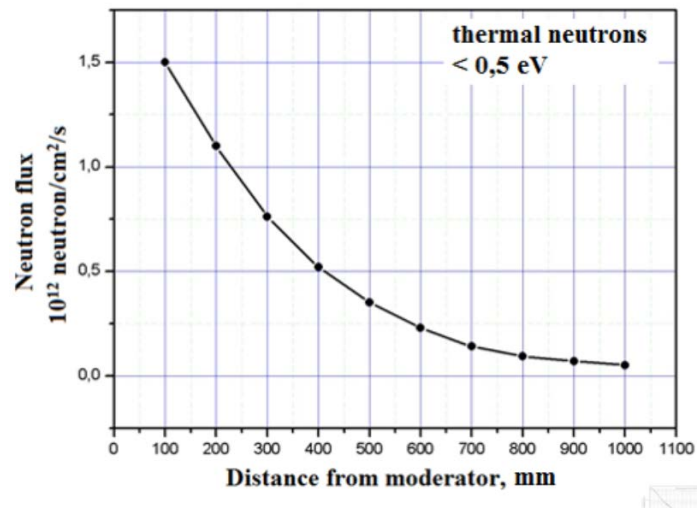
Figure 4.4. Flux of thermal neutrons to the distance from the moderator.
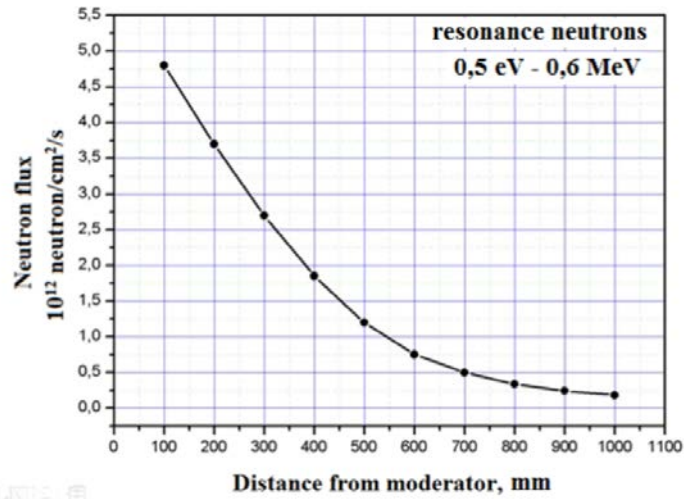
Figure 4.5. Flux of resonance neutrons to the distance from the moderator.
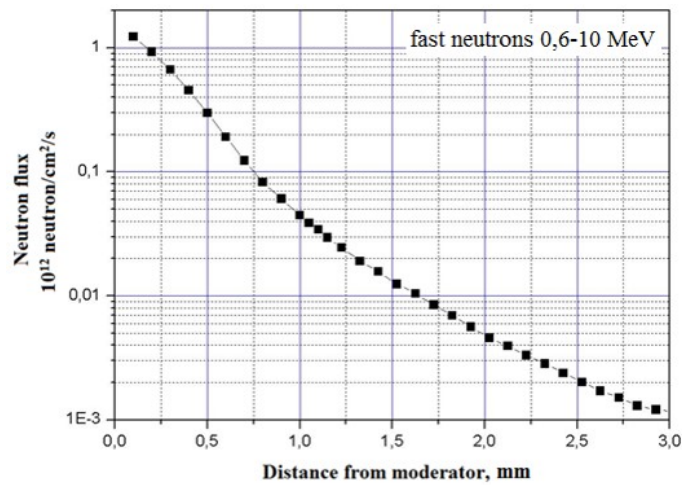
Figure 4.6. Flux of fast neutrons to the distance from the moderator.

Some of the samples were sent back to Airbus after irradiation to perform mechanical testing. Thus, this thesis only covers twelve of the samples, shown in Table 4.2. However, the results from the mechanical testing performed during this thesis will be compared to the results from Airbus.

To facilitate comparison of samples later on, the following nomenclature will be used:

Table 4.2. Nomenclature of specimens.

Radiation dose	Type A	Type B
0 MGy	#A0 top	#B0 top
0 MGy	#A0 mid	#B0 mid
0 MGy	#A0 bot	#B0 bot
3 MGy	#A3	#B3
10 MGy	#A10	#B10
30 MGy	#A30	#B30

5. Methodology

Firstly, examination of the homogeneity and distribution of the epoxy resin in irradiated and pristine CFRP samples was performed using X-ray and neutron tomography. The data were analysed by using a 3D reconstructed volume of each sample. Qualitative porosity analysis of the sample was performed by going through the reconstructed volume by hand, slice by slice. A quantitative porosity analysis was also performed by creating a MATLAB script. To determine how the mechanical properties of the samples are affected by radiation, mechanical testing was performed. Lastly, SEM was used to analyse the fracture surface.

5.1. Neutron Tomography

The neutron tomography was performed using the imaging instrument DINGO at ANSTO, Australian Nuclear Science and Technology Organisation, in Sydney. The DINGO instrument is illustrated in Figure 5.1. At ANSTO, a reactor is used to produce the neutrons before entering the moderator.

Thermal neutrons are ejected from the moderator and guided by a tube called the primary collimator [40]. A pinhole is used to produce a conically shaped beam with a nearly uniform intensity. Smaller diameter apertures increase the L/d ratio and improve the resolution of images. The distance L is measured from the pinhole to the scanned object [41].
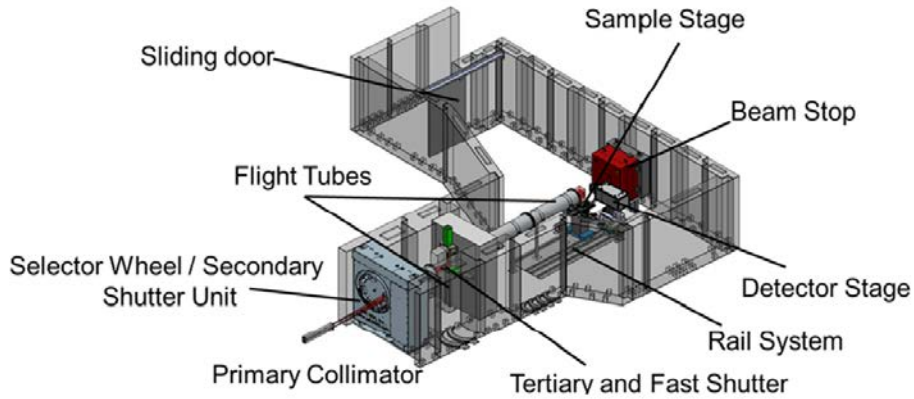
Figure 5.1. DINGO instrument assembly. Image taken from [42].

Since a large variety of samples are handled at ANSTO, the instrument is operated at two different beams; a high intensity beam and a high-resolution beam. To enable separation of these beams, a selector wheel is used to block one beam whilst the other is allowed to pass through the aperture to be used in the experiment. To avoid a reduced neutron flux due to air scattering, the flight tube between the selector wheel and sample shutter unit is filled with helium. The sample shutter unit includes two shutters; the main shutter and a fast shutter. These shutters work independently. The fast shutter is connected to the detector system and opens only when the detector is accumulating neutron radiation data. To reduce background radiation and protect the detector, the fast shutter is closed during the rest of the time. The main shutter regulates the access to the sample area and is thus part of the safety interlock system. After the main shutter, a second flight tube leads up to the sample stage [42].
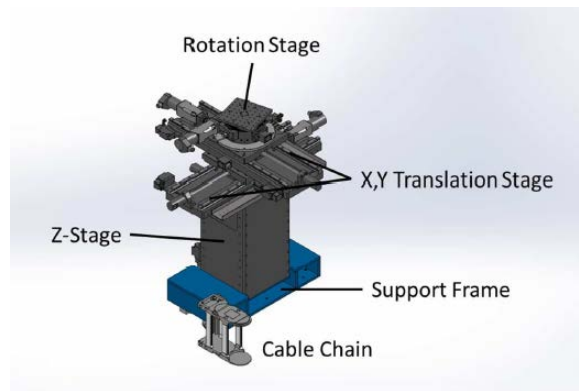

Figure 5.2. The rotation and translation stage of the DINGO instrument. Image taken from [42].

A xyz-translation table is required to position the sample in front of the detector. Moreover, the table is equipped with two high precision rotation stages needed for the neutron tomography, see Figure 5.2. To be able to fit three specimens at the rotation stage, they were placed in a shape of a triangle, see Figure 5.3.
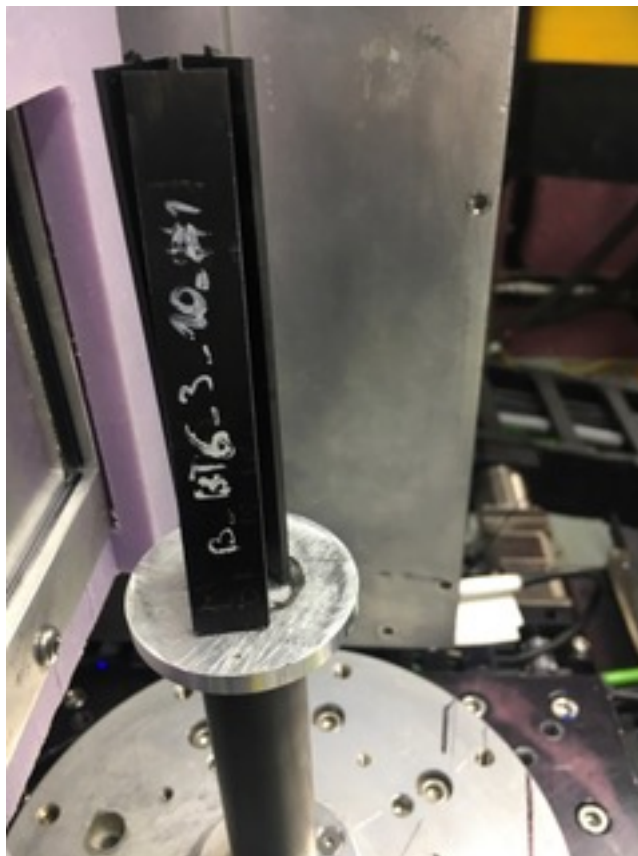
Figure 5.3. Placement of the samples during neutron tomography.

To enable positioning of the sample stage and the detector in the beam direction, they are mounted on a rail system. Thus, they can move independently. By moving the sample stage in the beam direction a preferable L/d ratio or beam size can be achieved [42].
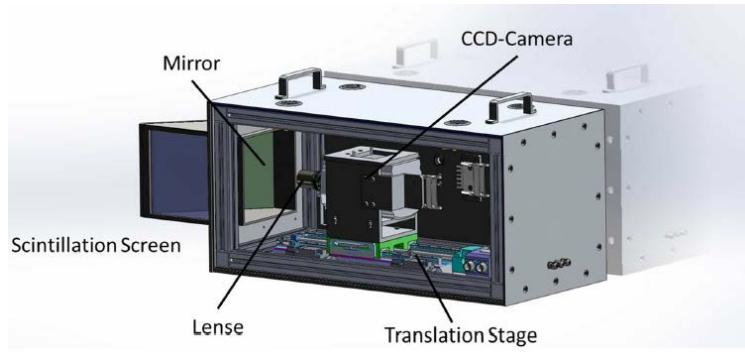
Figure 5.4. Detector box assembly of the DINGO instrument. Image taken from [42].

The major components of the detector box assembly are a scintillation screen, a mirror, and a CCD-camera as can be seen in Figure 5.4. The detector box is adjusted in the z-direction by translating between two fixed positions depending on the active beam. The scintillation screen is aligned to the beam and converts neutron radiation into visible light. The light is reflected by a mirror placed 45 degrees to the scintillation screen and then registered by the CCD-camera. Thus, the camera is placed out of the beam, at 90 degrees from the scintillation screen [42]. When the light reaches the charged-coupled device it will be converted into electrons. The number of collected electrons will be proportional to the intensity at each pixel [43].

To adjust the field of view based on the experimental conditions, the camera is mounted on a translation stage, see Figure 5.5. Thereafter, the camera box is closed and further functions of the camera, such as exposure time, can be controlled from the computer. Three pictures are taken at each angular position [42].
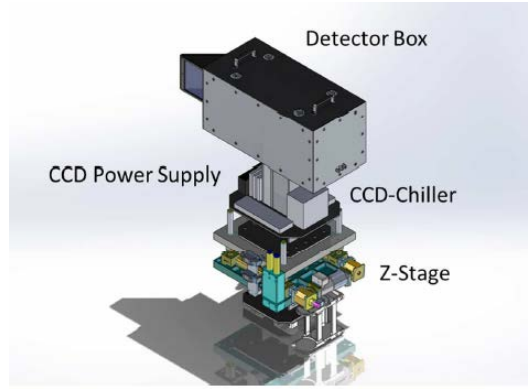
Figure 5.5. The detector box of the DINGO instrument is mounted on a translation stage. Image taken from [42].

5.1.1. Reconstruction Process

The reconstruction was made by the person responsible for the DINGO instrument at ANSTO. The raw data files were imported into ImageJ which is an image processing program based on Java. Using different threshold values in terms of pixels, outliers can be removed. Thereafter the image sequence was imported into a MATLAB-script which summarized the three pictures taken at each angle. The image sequences were then imported into MuhRec, a tool for computed tomography reconstruction. The images were normalised, i.e. variations in intensities were handled as described in section 3.6.4. Moreover, axis tilt was corrected for. Thereafter, sliced images parallel to the beam were created and beam hardening was corrected for.

5.2. X-ray Tomography

The X-ray tomography works in the same way as the neutron tomography explained in section 5.1. However, the neutrons are replaced by laboratory X-rays. Figure 5.6 shows the set-up of the experiment with the X-ray source, sample stage and detector. The X-ray source was operated at 60 kV. Furthermore, the length of one pixel in the images corresponds to 16μm.

The specimens were placed in groups of three, i.e. four data sets were measured. The specimens of each data set are shown in Table 5.1.

Table 5.1. Specimens in each data set for X-ray tomography.

Data set	Specimens		
1	#A0 top	#A0 mid	#A0 bot
2	#A3	#A10	#A30
3	#B0 top	#B0 mid	#B0 bot
4	#B3	#B10	#B30

To keep track of the specimens, a piece of paper was placed on the back of the top specimen. A plastic film was then used to wrap the specimens and keep them in place, see Figure 5.7.
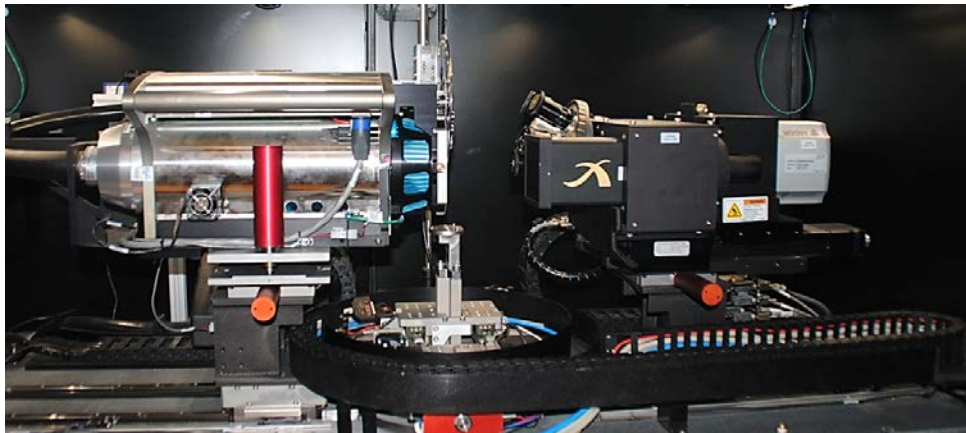
Figure 5.6. X-ray tomography set-up showing the X-ray source to the left and the detector to the right.
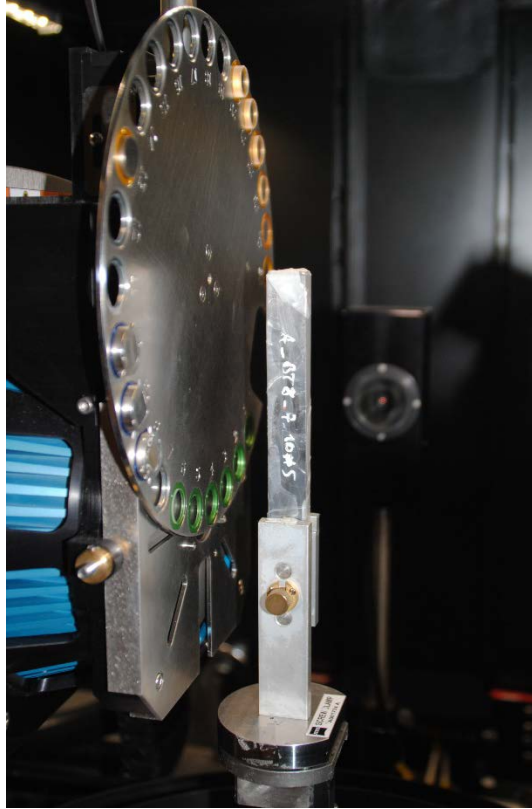
Figure 5.7. Samples wrapped in a plastic film to hold them in place during the X-ray tomography process.

5.3. Porosity Analysis

To analyse potential microstructural damage, MATLAB was used to create a program for image processing of the reconstructed data. One perpendicular slice of the reconstructed sample of one of the data set from the X-ray tomography is shown in Figure 5.8. The paper put on the sample to facilitate identification can be seen as well as the plastic film holding the samples in place.
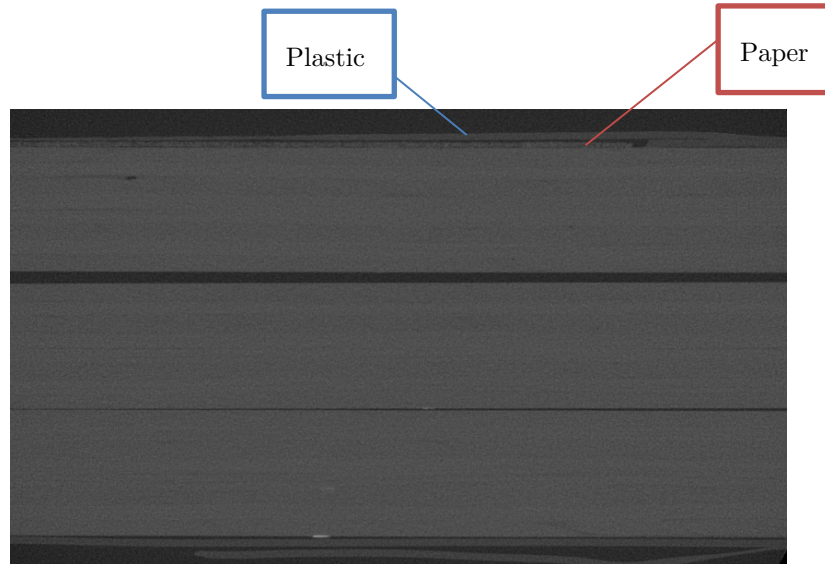
Figure 5.8. A perpendicular slice of the reconstructed data set. Three different samples are depicted, separated by dark black lines. The thin plastic wrap and the paper is shown on the top sample.

The first step of the script crops the specimens and places the images in individual folders, to enable a separate analysis of each specimen. For one data set, each folder thus contains 701 images of the top, middle, and bottom specimen, respectively.

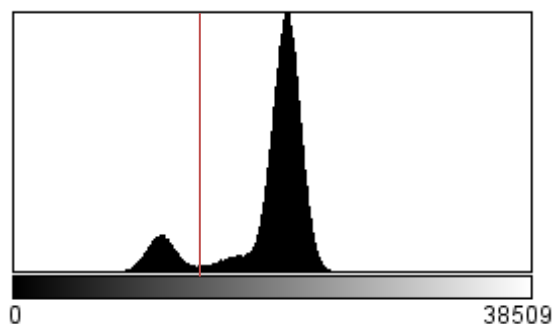Since pixel values are dependent on the level of attenuation of the material, allowing certain pixel values reveals what material each peak in the histogram corresponds to. The images are then binarized, with a threshold value set to include the pores.

Figure 5.9. A histogram of the grey scale values marked with the threshold value for binarization.

Hence, the pixels with a value lower than the threshold value will appear as white, while the others will appear as black. The top specimen from Figure 5.8, will thus look like Figure 5.10 after binarization.

Figure 5.10. Binarization of the top specimen from Figure 5.8 based on the threshold value.

The script then connects the voxels with the same value if their faces are adjacent. In addition, it calculates the number of voxels in each object and approximates the volume to an ellipsoid. Furthermore, the script extracts the axes of this ellipsoid. Hence, the ratio between the shortest and the longest axis will indicate the sphericity of the defect, zero being infinitely flat and one being perfectly round. The volume is returned as number of voxels. Furthermore, the diameter of the pore is calculated as the diameter of a sphere with the same volume as the region. Ratio and volume limits are set to define a pore, and thus reduce noise. Furthermore, the coordinates of each defect found using the script are extracted to enable comparison with the images. A more detailed explanation of the script is attached in Appendix B: MATLAB script.

5.4. Mechanical Testing

The three-point bending test was performed on a hydraulic mechanical testing machine, with a load cell capacity of 5000N. To eliminate air entrapment in the hydraulic system, the pump is used to adjust the position of the piston a couple of times. The ISO standard "SS-EN ISO 178:2010" is used as a template for the three-point bending test.

Since the flexural stress and strain are affected by the thickness and width of the specimen, they are measured using a micrometre calliper. The thickness and width of the specimens vary slightly throughout the specimens, and thus a mean value is presented in Table 5.2 below.

Table 5.2. Measurements of the specimens.

Specimen	Width w [mm]	Thickness h [mm]
#A0 top	15.28	2.16
#A0 mid	15.25	2.16
#A0 bot	15.23	2.16
#A3	15.21	2.22
#A10	15.22	2.15
#A30	15.21	2.18
#B0 top	15.25	2.24
#B0 mid	15.33	2.20
#B0 bot	15.27	2.21
#B3	15.22	2.22
#B10	15.28	2.19
#B30	15.35	2.20

Inserting values in equation (3.10) presented in the standard for calculating L gives:

$$L = (16 + 1) \times 2.2 \ = \ 37.4 \tag{5.1}$$

Thus, the distance L between the two supports are set to 40 mm, which is the shortest distance possible. The test speed was calculated according to equation (3.9).

$$v = \frac{1 \times 40^2}{600 \times 2.2} \approx 1.21 \tag{5.2}$$

The test speed was set to 1 mm/min.

The stress-strain curve was plotted using a MATLAB-script. Since the graph showed a curvature in the beginning, Young's modulus E_f was calculated by first observing the graph to make sure values at the linear part were extracted as shown in Figure 5.11, using equation (5.2).
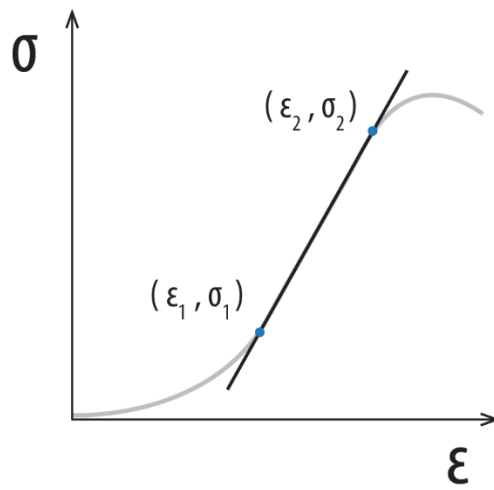
Figure 5.11. Illustration of the Young's modulus, i.e. the stiffness.

$$E_f = \frac{\sigma_2 - \sigma_1}{\varepsilon_2 - \varepsilon_1} \qquad (5.3)$$

Illustration of three-point bending is shown in Figure 5.12.
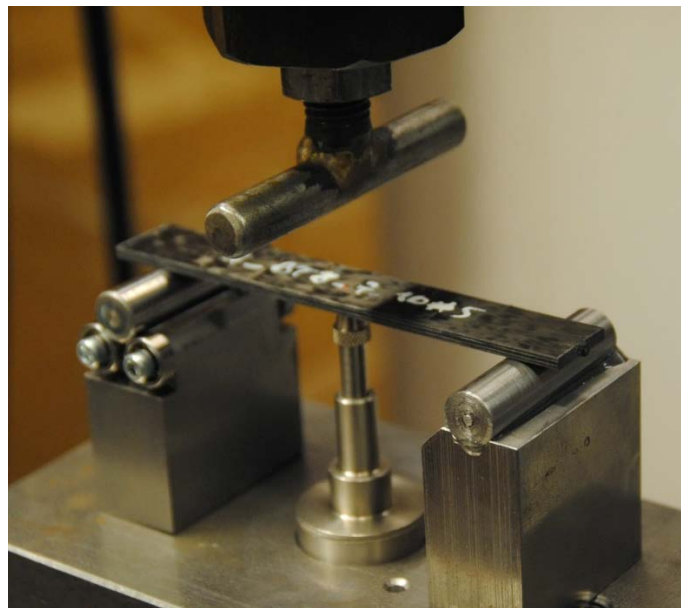
Figure 5.12. Illustrating three-point bending.

5.5. Scanning Electron Microscopy

To look at the fracture surface, a segment of one of the inner layers of the samples was investigated using SEM. The segments were mounted on the sample stage, according to Figure 5.12. Furthermore, the segments where attached using carbon tape to increase conductivity and avoid charging effects. The positions on the sample stage was numbered to keep track of each specimen.
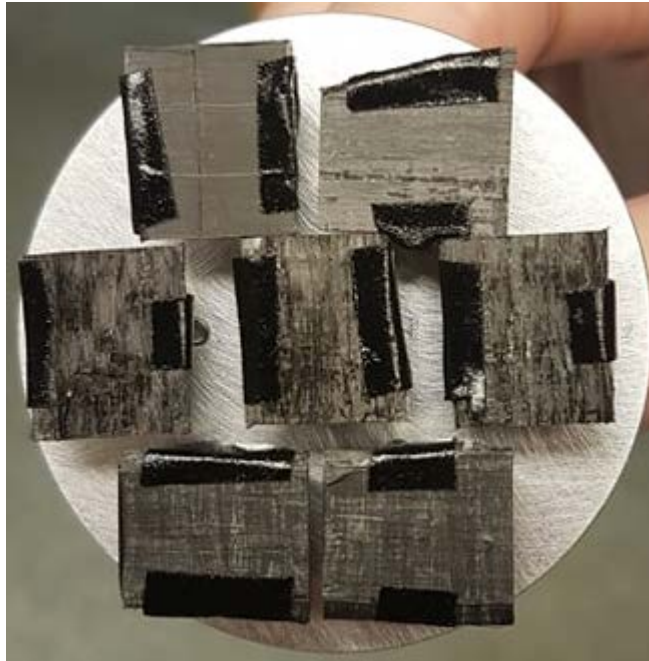
Figure 5.13. Sample segments mounted on the sample stage.

6. Result

6.1. Porosity Analysis

Since the reconstruction process of the neutron data got delayed due to the neutron facility, the porosity analysis presented below is only based on the X-ray tomography. The nomenclature of the samples was declared in section 4.

The number of detected pores for each sample is shown in Table 6.1.

Table 6.1. Number of pores detected in each sample.

Specimen	Number of pores
#A0 top	13
#A0 mid	12
#A0 bot	9
#A3	2
#A10	1
#A30	0
#B0 top	76
#B0 mid	63
#B0 bot	25
#B3	117
#B10	138
#B30	141

The diameter and ratio distribution of the detected pores are shown in Figure 6.1 and Figure 6.2, respectively. The yellow-red colour scheme indicates type A, while the grey-blue colour scheme represents type B. The higher the radiation dose, the darker the colour. Since three samples of each type are unirradiated, the mean value is plotted in each graph. However, error bars are placed on the mean value, showing the standard deviation.
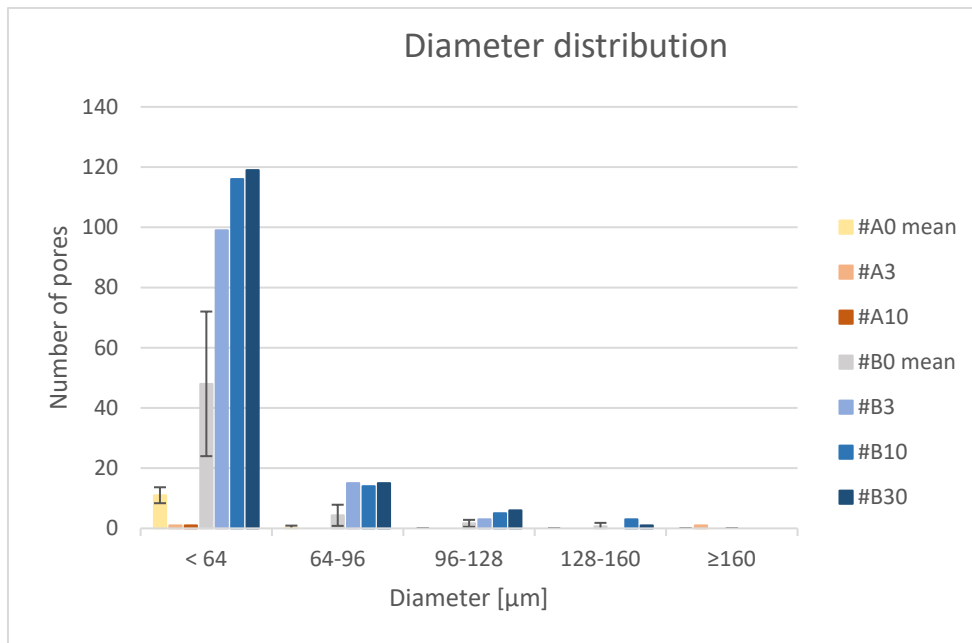
Figure 6.1. Diameter distribution of pores.
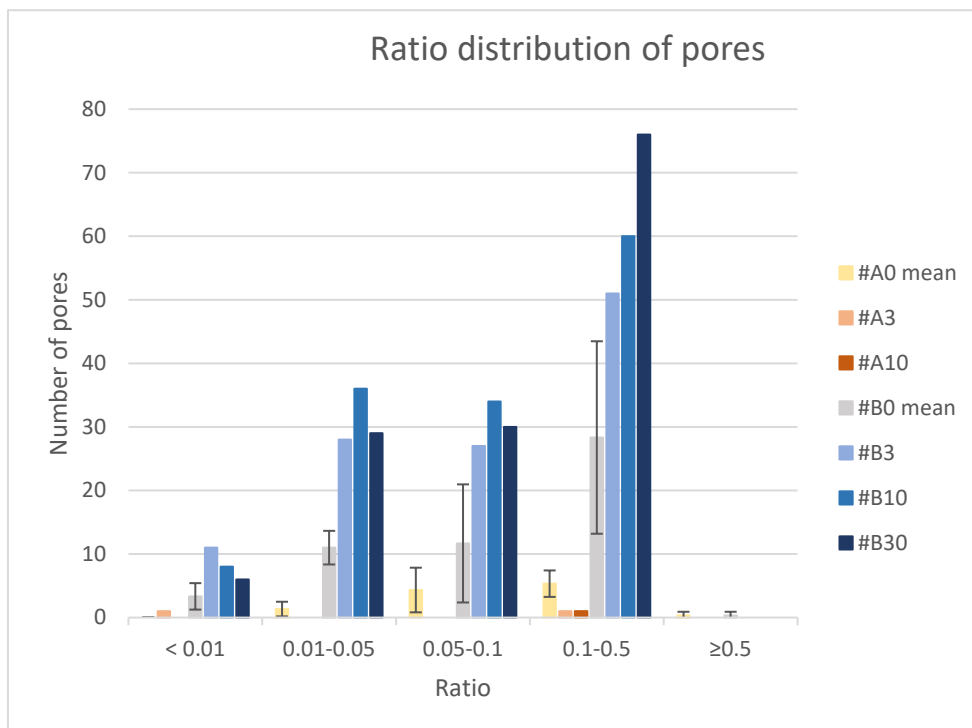
Figure 6.2. Ratio distribution of pores.

Figure 6.3 illustrates the shape of the pores, i.e. both ratio and volume. The graph is divided into nine areas, were each area represents a certain morphology of the pore in terms of ratio and size. Hence, it does not matter where the circles are positioned within each area. The size of the circles represents the number of pores having this specific morphology. Looking at the upper left area, i.e. large and flat defects, the mean value

of pores with this morphology found in the unirradiated type B samples is two. The #B3, #B10 and #B30 specimens have one, three and four pores, respectively with this specific morphology. The different areas are based on the volume and ratio limits displayed in Table 6.2 and Table 6.3, respectively.

Table 6.2. The volume limits used in Figure 6.3.

Definition	Volume interval [μm^3]	Corresponding number of voxels
Small	< 40960	< 10
Medium	40960 - 655360	10 -160
Large	≥ 655360	≥ 160

Table 6.3. The ratio limits used in Figure 6.3

Definition	Ratio interval
Flat	< 0.05
Elliptic	0.05 − 0.3
Round	≥ 0.3
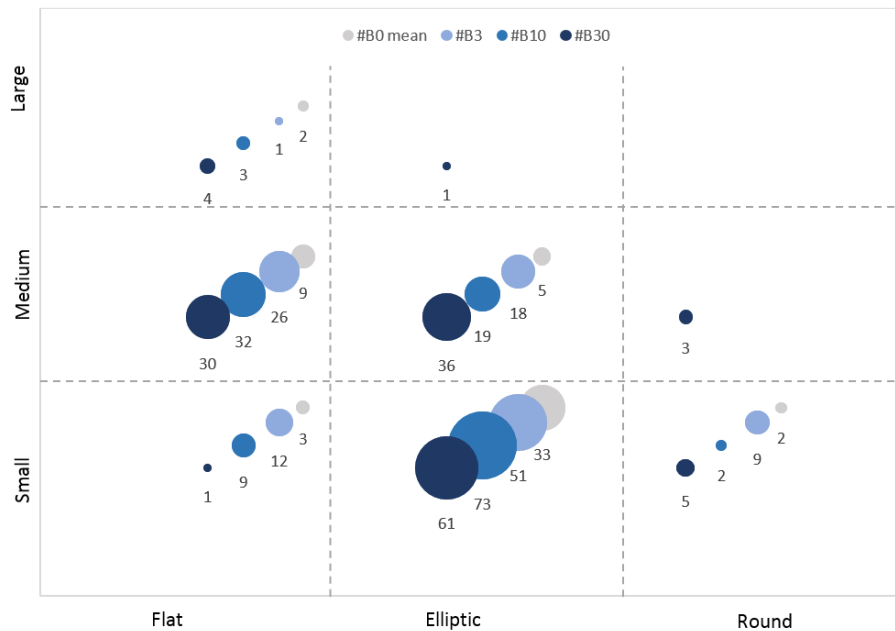
Figure 6.3. Illustration of the shape of the defects. The y-axis is based on the volume of the defect while the x-axis is based on the ratio.

Figure 6.4, Figure 6.5 and Figure 6.6 illustrates manual detection of a pore in the volume viewer of ImageJ.
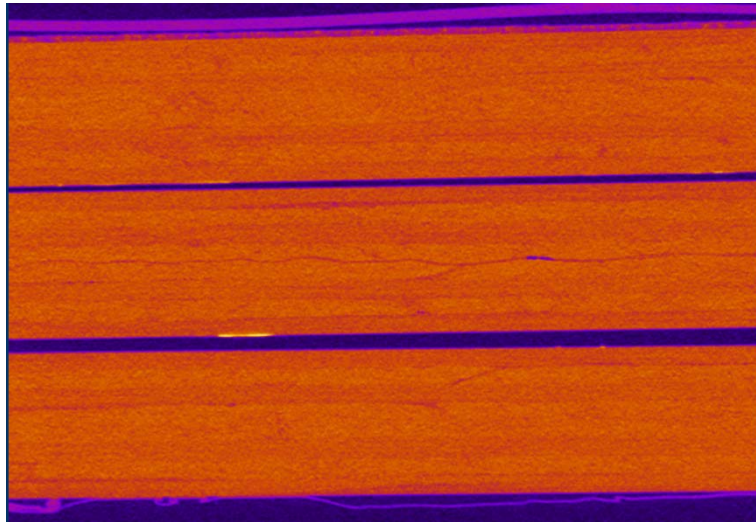
Figure 6.6. Samples during manual detection of pores.
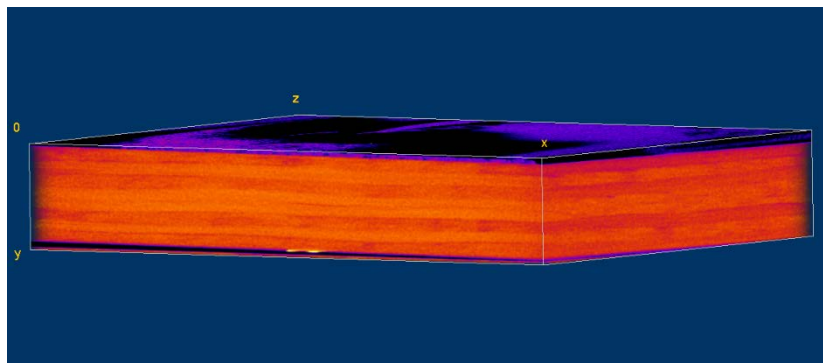
Figure 6.5. Example of a specimen showed in 3D during manual analysis of the samples.
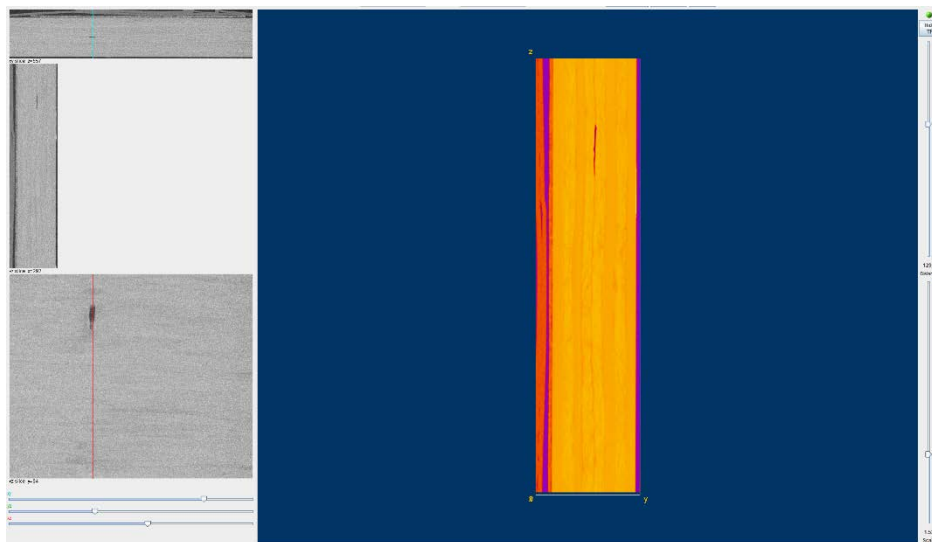
Figure 6.4. Example of a manually discovered defect in the volume viewer of ImageJ.

6.2. Mechanical Testing

The maximum stress at different radiation levels for type A and B samples are shown in Figure 6.5 and Figure 6.6, respectively.
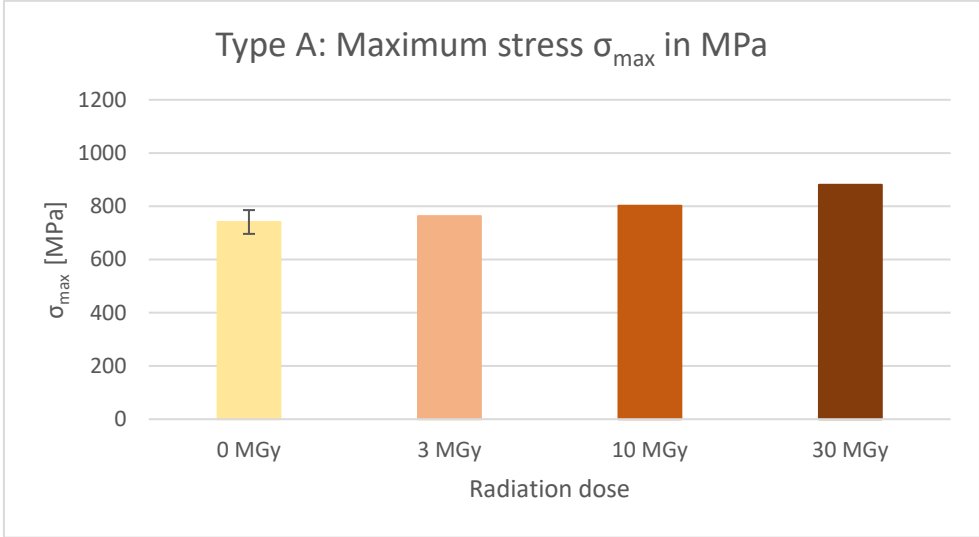
Figure 6.7. Maximum stress σmax in MPa to the radiation dose of the type A composite.
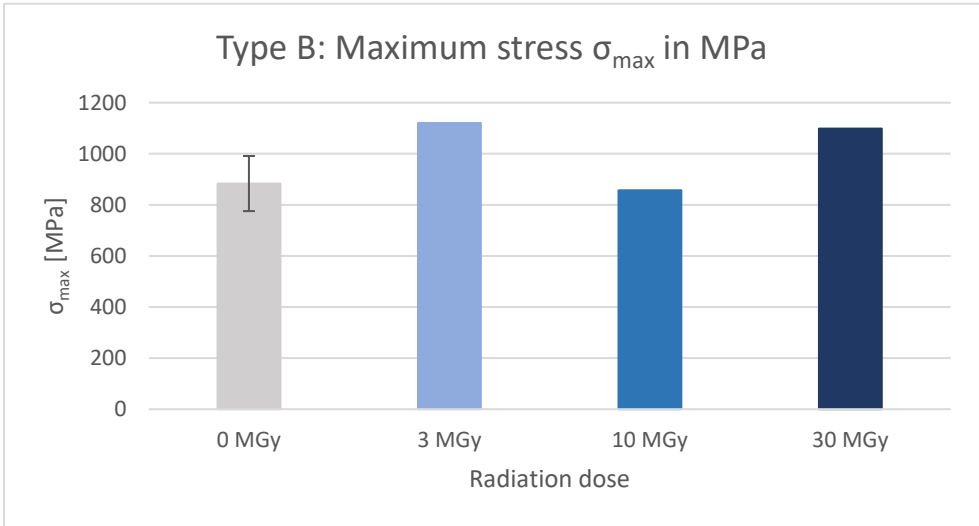
Figure 6.8. Maximum stress σmax in MPa to the radiation dose of the type B composite.

The E modulus at different radiation levels for type A and B samples are shown in Figure 6.7 and Figure 6.8, respectively.
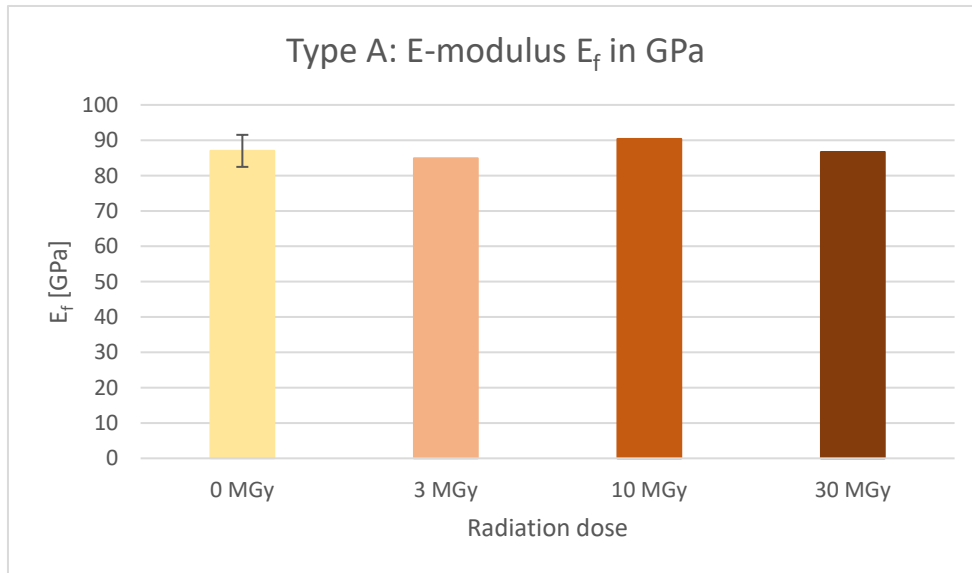
Figure 6.9. E modulus in GPa to the radiation dose of the type A composite.
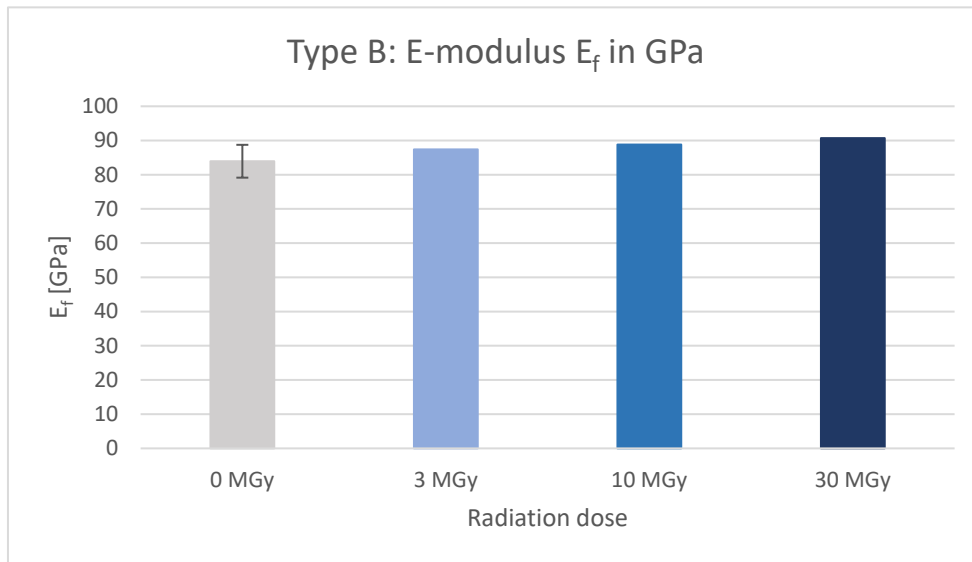
Figure 6.10. E modulus in GPa to the radiation dose of the type B composite.

The maximum strain at different radiation levels for type A and B samples are shown in Figure 6.9 and Figure 6.10, respectively.
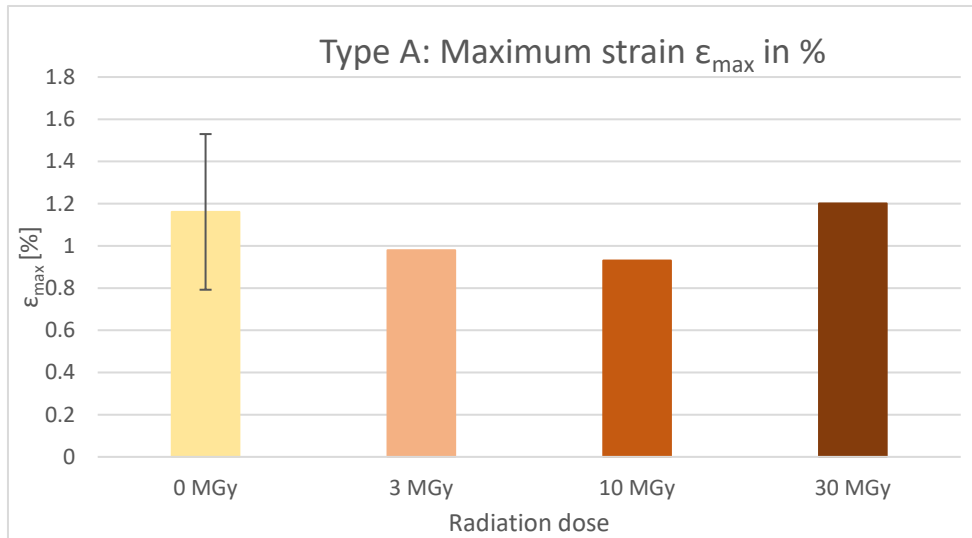
Figure 6.11. Maximum strain in % to the radiation dose of the type A composite.
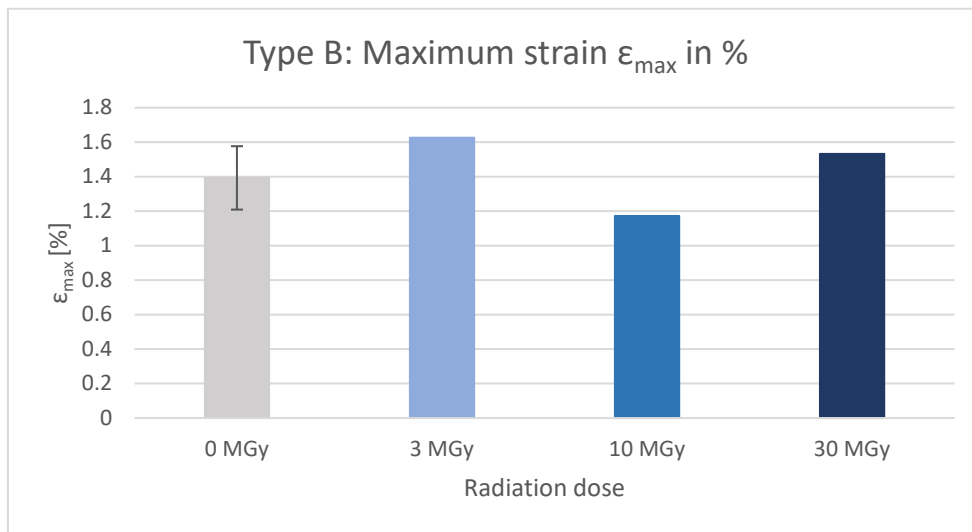
Figure 6.12. Maximum strain in % to the radiation dose of the type B composite.

The corresponding graphs to the mechanical tests are attached in appendix A.2 Graphs of the Mechanical Testing. Figure 6.11 shows a sample during the mechanical testing.
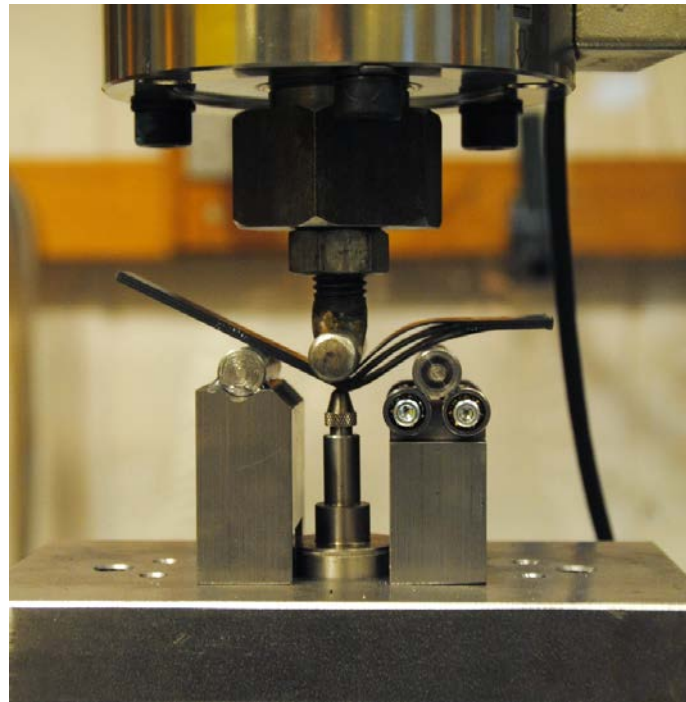
Figure 6.13. Three-point bending of sample.

6.3. Scanning Electron Microscope

To see the impact of radiation on the fracture surface, specimens irradiated with 30 MGy are compared with the unirradiated specimens. The images are shown at a magnification of 500 times. To facilitate comparison, the samples are shown adjacent
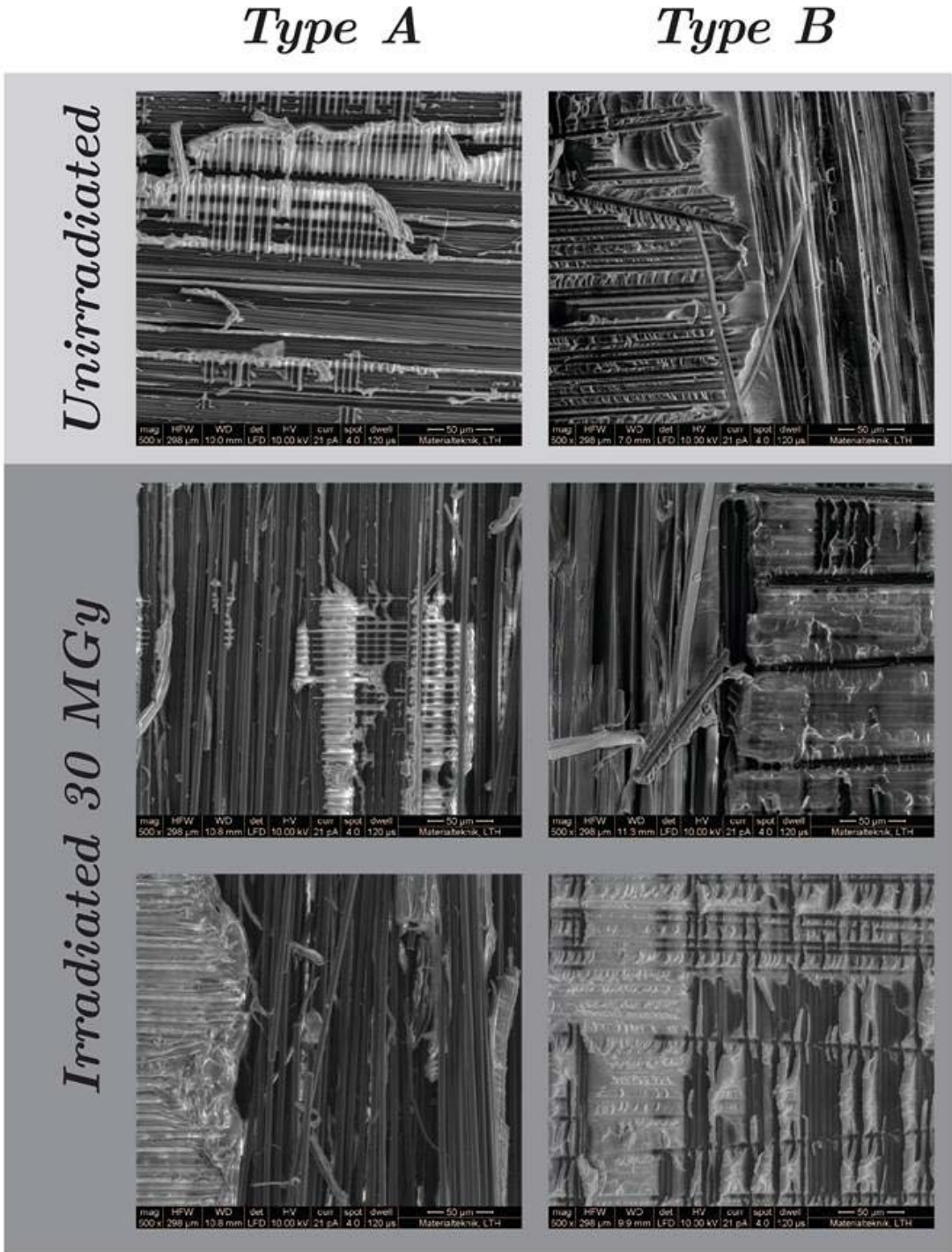
Figure 6.14. Comparison of fracture surfaces of type A and type B, both unirradiated and irradiated at 30 MGy.

to each other in Figure 6.12. Furthermore, the images in Figure 6.13 are parts of Figure 6.12 to show differences in fibres and epoxy between unirradiated and irradiated samples.
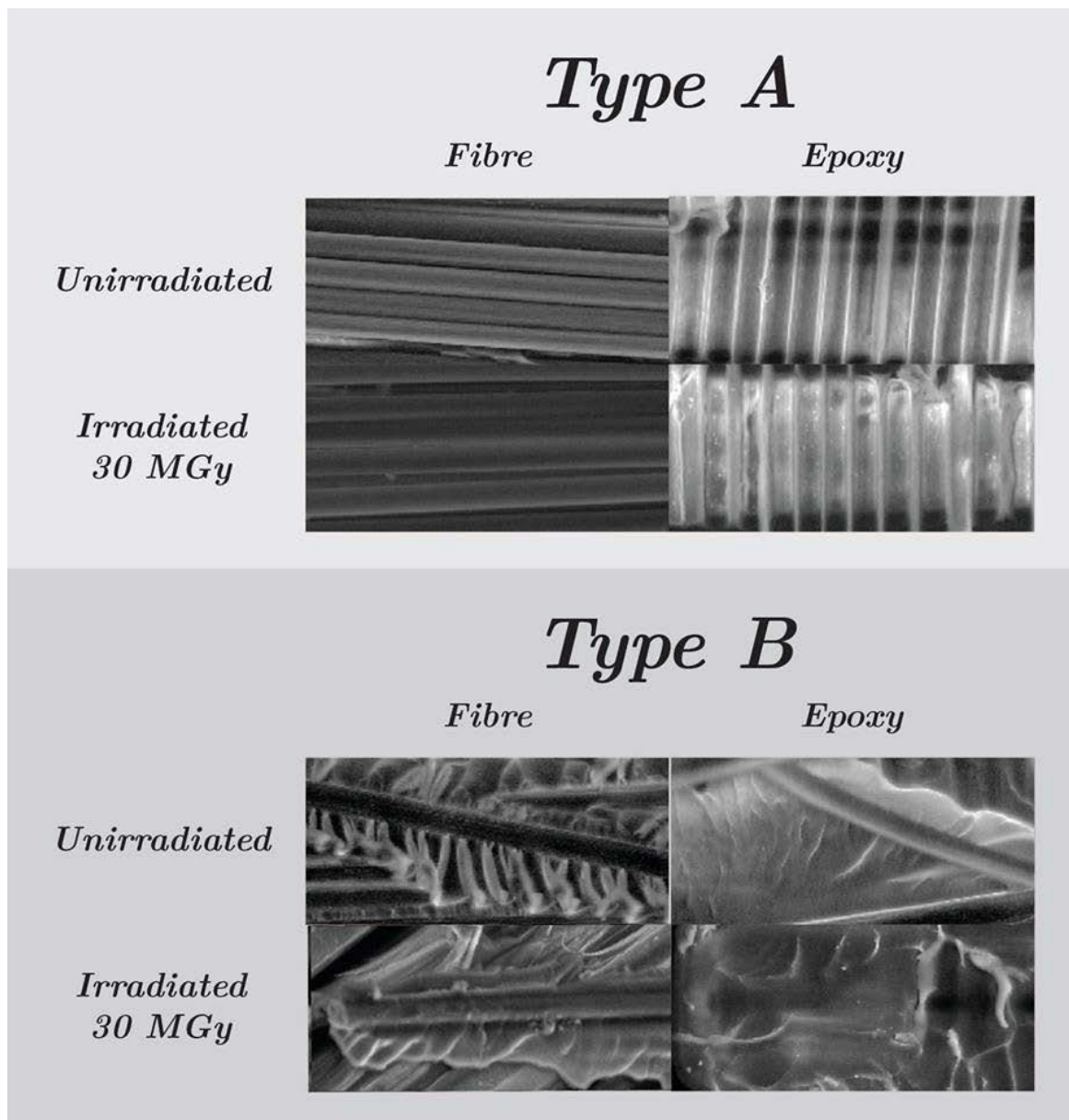
Figure 6.15. Comparison of fibres and epoxy between type A and type B for unirradiated and 30 MGy irradiated specimens.

The separate images from the SEM are attached in Appendix A.4 .

7. Discussion

Since several different analyses have been performed throughout this study, the discussion is divided into subsections.

7.1. Porosity Analysis

The MATLAB script detected the number of pores described in Table 6.1. To ensure the accuracy of the script, the pores were also manually detected using volume viewer in ImageJ. Using the coordinates of each pore from the script, it was possible to know that the script had detected all the pores in the samples. Looking at type A in Table 6.1 it looks as if the number of defects decreases with the radiation level. However, one should remember that the samples were milled out from different parts of the batch as discussed in section 4 and illustrated in Figure 4.1. This means that the risk of variety in terms of homogeneity of the material is higher. As discussed in the theoretical background in section 3.2, resins made of epoxy are relatively viscous which can result in difficulties impregnating woven fabrics. It is possible that the entrapped air was successfully removed in some parts of the batch, but not in all sections. Manufacturing defects like these explains why the unirradiated samples have defects. Inhomogeneity due to manufacturing defects could thus also be the reason why few, or no defects were found in the irradiated samples. To avoid manufacturing errors, it would have been optimal to analyse the porosity of some unirradiated samples, then irradiating these samples a certain dose and redo the porosity analysis to see what happened in the same samples. However, since the irradiated samples are radioactive, analysis cannot be performed until the radioactivity has declined to safe levels for humans which could take up to several years. Thus, performing repeated analyses of the same samples would require an unfeasible amount of time for this study. Since the porosity analysis did not reveal many pores in type A, the rest of the discussion will mainly focus on the type B samples.

Looking at Figure 6.1, it is seen that the number of pores with a diameter < 64 µm increases with radiation dose. The number of pores in the #B3 sample in this interval

is above the upper error bar of the #B0 mean value. However, the relative increase seems to stagnate slightly between the #B10 and #B30 sample. In order to see whether this trend is real it would have been a good idea to analyse more than one sample at each radiation level. Furthermore, it would be interesting to see what happens at doses higher than 30 MGy. As mentioned before, it would have been difficult to irradiate the samples with higher levels due to the time it takes for the samples to reach a safe level after irradiation. In any case, a significant increase of pores with a diameter < 64 µm is seen. In addition, the number of pores seems to increase slightly in the interval 96-128 µm. However, in this case the trend is not as strong since there are only a few pores within this interval, making it difficult to draw any conclusions.

Looking at Figure 6.2 it is seen that pores with ratios between 0.1 and 0.5 seem to increase with radiation dose. With the same reasoning as before, the number of pores in the #B3 sample in this interval is above the upper error bar of the #B0 mean value indicating a significant trend. Furthermore, there are a lot of pores present in this region which also supports the indication. In addition, it is seen that the pores in the samples are not very round, but rather elliptic.

In Figure 6.3, three of the fields are more dominating; flat-medium sized, elliptic-medium sized, and elliptic-small sized. Looking at the elliptic-medium sized pores, i.e. the field in the middle, there seems to be an increasing trend of these types of pores as the radiation dose increases. This graph is interesting in order to understand the radiation damage further. It maps out the morphology of the pores which would indicate what happens with already existing pores; do they expand horizontally or vertically with radiation? Or perhaps it is favourable to create new pores rather than expanding the pre-existing pores. If the latter claim was true, the circles should expand at the lowest row in the graph as the radiation dose increases. However, this trend is not seen. On the contrary, the lower left area i.e. flat-small sized pores almost seem to decrease with radiation dose. That could indicate that the pores of this morphology have grown horizontally, vertically or both. Detection of certain trends and significant changes would have been facilitated and more reliable if multiple samples at each radiation dose were analysed.

7.1.1. Radiation Mechanism

As described in the theoretical background, in sections 3.2, 3.4.2 and 3.5, the pores in the material can be a result of radiation decomposition phenomenon or off-gassing of the epoxy due to post-curing. However, the placement and morphology of the pores could be a result of two different mechanisms;

1) *Absorption cross section*

   Before radiation exposure the material exists in a solid state, with a certain element composition and thus also a certain absorption cross section $\sigma_{material}$. However, elements with a high absorption cross section, such as hydrogen, will absorb more energy from neutrons and convert it to heat. If radiation deposits enough energy in the epoxy it will gasify, i.e. epoxy is converted to gas. Furthermore, if the absorption cross section of this gas σ_{gas} is greater than the cross section for the rest of the material $\sigma_{material}$ it would absorb even more heat and thus expand. Hence, if $\sigma_{gas} > \sigma_{material}$ the pre-existing pores would expand rather than forming new pores.

2) *Surface effect*

   As the defect absorbs more heat, it will grow and thus increase the surface area. Thus, the probability to absorb even more heat increases, and the defect will continue to grow.

7.2. Mechanical Testing

Firstly, to see if the results from the mechanical testing are reasonable, they are compared to the results from AIRBUS, see appendix A.1 AIRBUS RESULTS. It should be noted that AIRBUS used a length between the supports of L = 80 mm and not L = 40 mm as in this study. Furthermore, AIRBUS uses a test speed of v = 2 mm/min, while in this study the test speed was set to v = 1 mm/min.

Comparing the maximum stress for type A in Figure 6.5 and Figure A.1, the results are quite consistent although AIRBUS values are slightly higher. Furthermore, observing the results from this study, there seems to be a small increase of maximum stress in type A with an increased radiation dose. This trend is also seen in the graph

from Airbus until the #A30. One should keep in mind that the maximum stress is affected by the width and thickness of the sample. The latter parameter having a bigger impact, as seen in equation (3.8). Thus, errors in measurements will have a big impact on the results. Furthermore, as discussed in section 3.2.1, failure will occur in the weakest part of the composite. Thus, if the reinforcement is not placed evenly throughout the composite, the reinforcement-poor areas will be much weaker which can result in early crack initiation. Furthermore, as mentioned before, other manufacturing parameters such as curing of epoxy and entrapment of air can impact the mechanical properties of the material. No trend is seen when comparing the maximum stress for type B, see Figure 6.6 and Figure A.1.

When comparing the E-modulus values of type A and B in Figure 6.7 and Figure 6.8 to the E-modulus measured by Airbus in Figure A.1.2, the E-modulus measured by Airbus are generally higher. However, Airbus does not show how the E-modulus was calculated nor the measured stress-strain graph. This makes comparison difficult. The type B E-modulus measured in this study seems to increase with radiation dose, i.e. the material seems to get stiffer with increased radiation dose. This could be due to the increasing number of pores in the material, making the CFRP more brittle. However, looking at the E-modulus measured by Airbus the overlapping error bars indicate that the difference is probably not statistically significant.

It is possible that the differences in the mechanical tests are due to the different set-ups. Since Airbus used twice the test speed of this study, it is possible that their samples appeared a bit stiffer than the samples tested in this study.

The graph showing the corresponding strain at the maximum stress for type A and B, see Figure 6.9 and Figure 6.10, is similar to Airbus graph in Figure A.1.3. The values of type A from this study lies within the error bars of Airbus measurements, except for #A30. Furthermore, both the measurements in this study and the measurements from Airbus show that type B generally elongates more than type A. However, there is a big variance in the result making it difficult to draw any conclusions. Furthermore, the error bars are overlapping indicating that the difference is not statistically significant. Intuitively, one might expect the mechanical properties of type B to worsen with radiation due to the increasing number of pores in the material. However, many aspects except the number of pores are to be considered. Firstly, as mentioned in section 4, samples are extracted from different parts of the batch which would increase the risk

of variance in the structure and thus also the mechanical properties. Furthermore, the radiation might induce cross-linking to occur in the epoxy making the material stiffer and stronger. Another aspect to consider is the toughening mechanisms acting within the material. Fibre bridging, matrix cracking and debonding of fibres all help crack retardation. Thus, it is difficult to draw conclusions by solely looking at the mechanical testing. However, it is clear from Figure 6.11 that delamination of the specimen occurs during testing. It can also be seen that different macroscopic modes are present as the top layers are put through compression while the bottom part experiences tension. Furthermore, the layers in between experience shear forces.

7.3. Scanning Electron Microscopy

Comparing the fibres in the unirradiated and 30 MGy irradiated samples of type A, i.e. #A0 and #A30, they are very similar as can be seen in Figure 6.12 and Figure 6.13. There is no evident epoxy attached to the fibres in #A0 nor #A30. In addition, the concave channel structure of the epoxy of type A shown in Figure 6.13 suggests that debonding has occurred since the fibres have been pulled-out without detaching the epoxy. Thus, the failure seems to be adhesive indicating a weak interface between the matrix and fibres. As discussed in section 3.2.1 this indicates that the material has a high fracture resistance but produces a lower stiffness and strength. The unirradiated sample in the previous study seems to have more matrix debris on the fibres, see Figure 3.15. Furthermore, the matrix of the unirradiated sample in the previous study showed a more dimpled fracture surface, while the irradiated showed clear matrix cracks, see Figure 3.18.

Comparison of the fibres in the unirradiated and 30 MGy irradiated samples of type B, i.e. #B0 and #B30, is difficult due to the lack of fibres seen in the fracture surface. However, the fibre of #B0 shown in Figure 6.13 reveals no or minimal epoxy attached, while the fibre of #B30 is still attached to the matrix. Furthermore, the epoxy behind the fibres show a bit brittle structure with facets indicating a more cohesive failure. Comparing the epoxy of #B0 and #B30, they both have a similar groove structure. However, the groove structure seems to be a bit deeper in #B30. The epoxy structure of the type B samples appears to be somewhat similar to the one seen in the previous study, see Figure 3.17 and Figure 3.18.

Thus, there are not many differences to observe between different radiation doses within each composite type. Instead, more differences are observed between type A and B. If type A generally has adhesive failure and type B shows a cohesive failure it would be consistent with the higher strength and stiffness observed in type B. However, more segments and other layers of the specimens should be analysed to draw any further conclusions. Furthermore, the previous study used a tilted angle during the SEM as opposed to this study. Using a tilted angle would facilitate the observation of facets and cracks in the matrix.

8. Conclusion

In this master's thesis, the effects of radiation on CFRP used in neutron chopper discs have been investigated. Many different experimental techniques have been included, to enable analysis of both the microstructural and mechanical properties. From the X-ray tomography in combination with the MATLAB-script, it can be concluded that number of pores increases with radiation dose. However, this effect is not universal between different types of resins. Furthermore, a certain morphology of the pores seems to be favourable, which is the elliptic medium sized. The mechanical properties were analysed by three-point bending. However, no significant trend with increased radiation dose was detected within the mechanical properties. SEM revealed no evident structural changes at different radiation levels.

9. Further Work

As the reconstruction process of the neutron data got delayed, it was not possible to include a porosity analysis based on the neutron tomography due to the time constrictions of this project. However, it was possible to detect an increase of pores by only analysing the X-ray data. The next step of this project would be to analyse the neutron data to see if this trend is visible there as well. Furthermore, the neutron data would be able to provide additional information on the gas inside the pores, since X-rays and neutrons have different cross-sections.

In addition, the radiation mechanism can be investigated further. One way of gaining more knowledge of the radiation mechanisms could be to analyse the orientation of the pores. This could be done to see whether they are aligned in a certain direction, such as along the weave. In addition, further investigation could be made using SEM to analyse more segments of the specimens.

10. References

[1]   K. Andersen *et al.*, *ESS Conceptual Design Report.* European Spallation Source (ESS),, 2012.

[2]   The European Spallation Source, The European Spallation Source | ESS. [Online]. Available: https://europeanspallationsource.se/about. Accessed on 17 February 2019.

[3]   Spallation Neutron Source, Spallation—What and Why, 2004,. [Online]. Available: https://web.archive.org/web/20060904163514/http://www.sns.gov/aboutsns/what-why.htm. Accessed on 28 November 2018.

[4]   M. Åberg *et al.*, ESS Technical Design Report, S. Peggs, ed.: European Spallation Source, 2013. [Online]. Available: http://europeanspallationsource.se/documentation/tdr.pdf. Accessed on 21 December 2018.

[5]   N. Tsapatsaris, "Definitions of terms (DoT) document for neutron chopper systems."

[6]   M. H. Hassan, A. Othman, and S. Kamaruddin, *A review on the manufacturing defects of complex-shaped laminate in aircraft composite structures.* 2017.

[7]   N. Tsapatsaris, "ESS-0061574 Projectile analysis for Neutron Choppers Systems in the ESS Instrument suite."

[8]   E. Nilsson, "ESS-0041176 Requirements specification for CHIM, Horizontal split DC-SR."

[9]   F. L. Matthews and R. R.D., *Composite materials: Engineering and science.* Cambridge, United Kingdom: Woodhead Publishing Limited, 2008.

[10]   A. Sjögren, Composite materials design, Lund University, 2018. [Online]. Available: https://liveatlund.lu.se/departments/MachineDesign/MMKN41/MMKN41_2018VT_100_1_NML__1281/CourseDocuments/Lecture%202.pdf. Accessed on 27 December 2018.

[11]   S. R. Clarke, "Net Shape Woven Fabrics—2D and 3D," *Journal of Industrial Textiles,* vol. 30, no. 1, pp. 15-25, 2000/07/01 2000.

[12]   X. Dai, Y. Wang, C. Tang, and X. Guo, "Mechanics analysis on the composite flywheel stacked from circular twill woven fabric rings," *Composite Structures,* vol. 155, pp. 19-28, 2016/11/01/ 2016.

[13]   M. Naebe, M. M. Abolhasani, H. Khayyam, A. Amini, and B. Fox, "Crack Damage in Polymers and Composites: A Review," *Polymer Reviews,* vol. 56, no. 1, pp. 31-69, 2016/01/02 2016.

[14]   K. B. Broberg, "1 - The Process Region," in *Cracks and Fracture*, K. B. Broberg, Ed. San Diego: Academic Press, 1999, pp. 5-26.

[15]   B. N. Cox, M. S. Dadkhah, W. L. Morris, and J. G. Flintoff, "Failure mechanisms of 3D woven composites in tension, compression, and bending," *Acta Metallurgica et Materialia,* vol. 42, no. 12, pp. 3967-3984, 1994/12/01/ 1994.

[16]   G. Han, Z. Guan, X. Li, R. Ji, and S. Du, "The failure mechanism of carbon fiber-reinforced composites under longitudinal compression considering the interface," in *Science and Engineering of Composite Materials* vol. 24, ed, 2017, p. 429.

[17]   J. Hornikova and m. a biomechaniky Vysoké učení technické v Brně. Ústav mechaniky těles, *Shielding effects at the crack front = Účinky stínění na čele trhliny : teze habilitační práce.* 2019.

[18]   U. S. D. o. Energy, "DOE Fundamentals handbook nuclear physics and reactor theory," vol. 1.

[19]   The European Spallation Source, The ESS Mandate. [Online]. Available: https://europeanspallationsource.se/ess-mandate. Accessed on 3 January 2019.

[20]   Health Physics Society, Gray. [Online]. Available: http://hps.org/publicinformation/radterms/radfact79.html. Accessed on 21 October 2018.

[21]   K. E. Holbert, Radiation effects and damage, 2007. [Online]. Available: http://holbert.faculty.asu.edu/eee560/RadiationEffectsDamage.pdf. Accessed on 10 November 2018.

[22]   National aeronautics and space administration, "Nuclear and space radiation effects on materials," 1970.

[23] T. Šarac, N. Quiévy, A. Gusarov, and M. J. Konstantinović, "Influence of γ - irradiation and temperature on the mechanical properties of EPDM cable insulation," *Radiation Physics and Chemistry,* vol. 125, pp. 151-155, 2016/08/01/ 2016.

[24] E. N. Hoffman and T. E. Skidmore, "Radiation effects on epoxy/carbon-fiber composite," *Journal of Nuclear Materials,* Article vol. 392, pp. 371-378, 1/1/2009 2009.

[25] R. Pynn, "Neutron scattering - a primer," *Los Alamos Science Center,* 1990.

[26] J. Banhart *et al.*, *X-ray and neutron imaging - Complementary techniques for materials science and engineering.* 2010, pp. 1069-1079.

[27] Paul Scherrer Institute, Neutron imaging at the spallation source SINQ. [Online]. Available: https://www.psi.ch/niag/ImagingBrochureEN/Neutron_Imaging_User_2016.pdf. Accessed on 20 October 2018.

[28] J.-y. Buffiere, E. Maire, J. Adrien, J.-P. Masse, and E. Boller, *In Situ Experiments with X ray Tomography: An Attractive Tool for Experimental Mechanics.* 2010, pp. 289-305.

[29] M. Raventos, R. P. Harti, E. Lehmann, and C. Grünzweig, "A Method for Neutron Scattering Quantification and Correction Applied to Neutron Imaging," *Physics Procedia,* vol. 88, pp. 275-281, 2017/01/01/ 2017.

[30] R. Ketcham, X-ray Computed Tomography (CT), Carleton college: Science education resource centre, 2017. [Online]. Available: https://serc.carleton.edu/research_education/geochemsheets/techniques/CT.html. Accessed on 21 November 2018.

[31] F. Boas and D. Fleischmann, *CT artifacts: Causes and reduction techniques.* 2012.

[32] R. Ketcham and W. D. Carlson, *Acquisition, optimization and interpretation of X-ray computed tomographic imagery: Applications to the geosciences.* 2001, pp. 381-400.

[33] Z. Kiss, L. Rodek, and A. Kuba, "Image reconstruction and correction methods in neutron and X-ray tomography " vol. 17, no. 3, pp. 557-587, 2006.

[34] P. E. Optics, *Environmental Scanning Electron Microscopy: An Introduction to ESEM.* Philips Electron Optics, 1996.

[35]   Microscopy Australia, Scanning Electron Microscopy. [Online]. Available: https://myscope.training/#/SEMlevel_2_20. Accessed on 10 March 2019.

[36]   D. D. F. Adams, Flexural testing of composite materials: CompositesWorld, 2013. [Online]. Available: https://www.compositesworld.com/articles/flexural-testing-of-composite-materials(2). Accessed on 11 November 2018.

[37]   *Plastics – Determination of flexural properties (ISO 178:2010)*, 2011.

[38]   C. Geschke, "Irradiation of Resin and CFRP used for Airbus Chopper Systems," AIRBUS2017, vol. 2.

[39]   A. Munter, Neutron scattering lengths and cross sections, National Institute of Standards and Technology Center for Neutron Research,, 2013. [Online]. Available: https://www.ncnr.nist.gov/resources/n-lengths/. Accessed on 11 March 2019.

[40]   Australian Nuclear Science and Technology Organisation, Technical Information - Dingo. [Online]. Available: https://www.ansto.gov.au/research/user-office/instruments/neutron-scattering-instruments/dingo/technical-information. Accessed on 16 October 2018.

[41]   National Institute of Standards and Technology, Neutron Imaging Facility, 2004. [Online]. Available: https://physics.nist.gov/MajResFac/NIF/facility.html. Accessed on 17 October 2018.

[42]   U. Garbe, T. Randall, C. Hughes, G. Davidson, S. Pangelis, and S. J. Kennedy, "A New Neutron Radiography / Tomography / Imaging Station DINGO at OPAL," *Physics Procedia,* vol. 69, pp. 27-32, 2015/01/01/ 2015.

[43]   C. McFee, An introduction to CCD operation: Mullard Space Science Laboratory. [Online]. Available: http://www.mssl.ucl.ac.uk/www_detector/ccdgroup/optheory/ccdoperation.html. Accessed on 11 November 2018.

[44]   K. Pandya, C. V. Sesha Kumar, N. Nair, P. Patil, and N. Naik, Analytical and experimental studies on ballistic impact behavior of 2D woven fabric composites. 2014.

[45]   G. Han, Z. Guan, X. Li, R. Ji, and S. Du, "The failure mechanism of carbon fiber-reinforced composites under longitudinal compression considering the interface," in Science and Engineering of Composite Materials vol. 24, ed, 2017, p. 429.

Appendix A: Mechanical Testing

A.1 AIRBUS RESULTS

The maximum stress, E-modulus and maximum strain are illustrated in Figure A.1, Figure A.1.2 and Figure A.1.3, respectively. To facilitate comparison, the colour coding of the graphs is the same as the results in this study, see section 7.2. Furthermore, the test speed of Airbus was set to v = 2 mm/min and the distance between the supports was set to L = 80 mm.
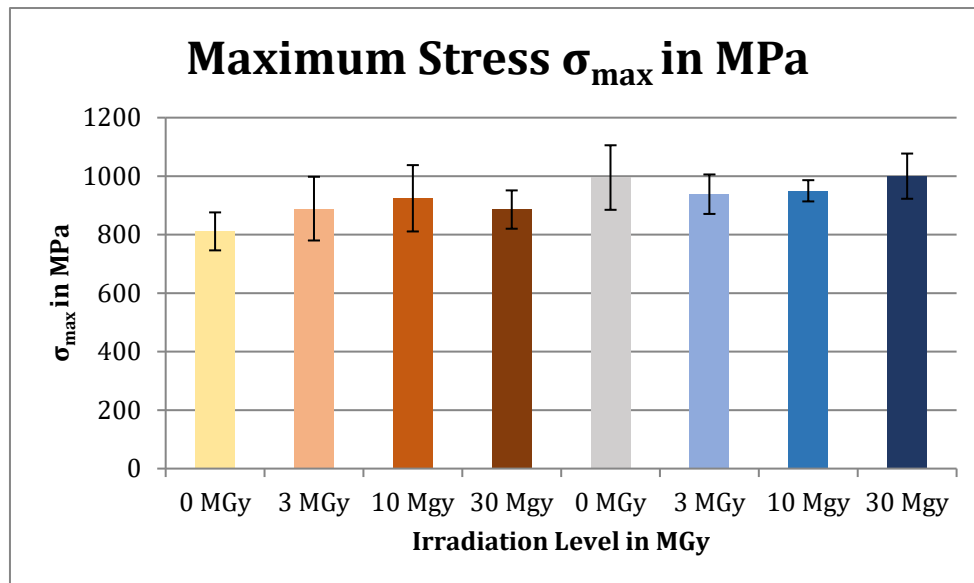

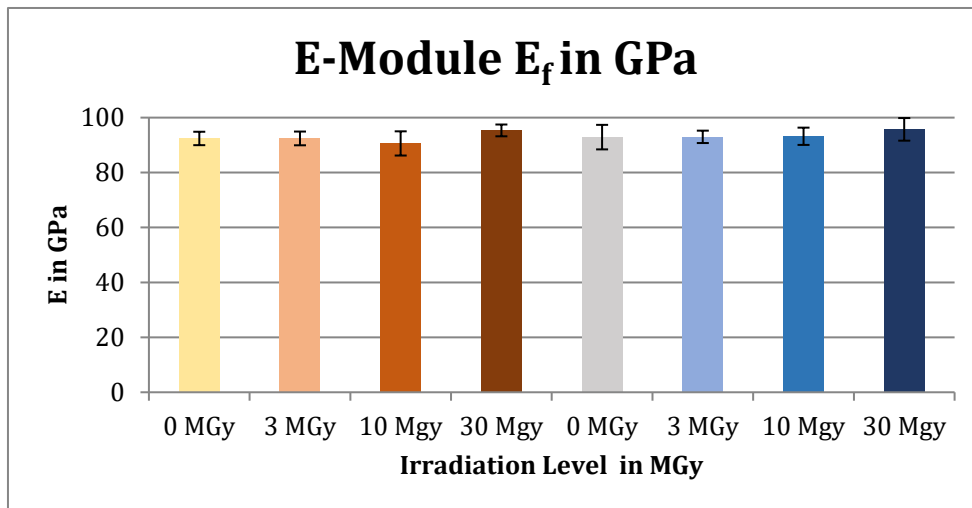**Figure A.1.1. Maximum stress in MPa, measured by Airbus.**

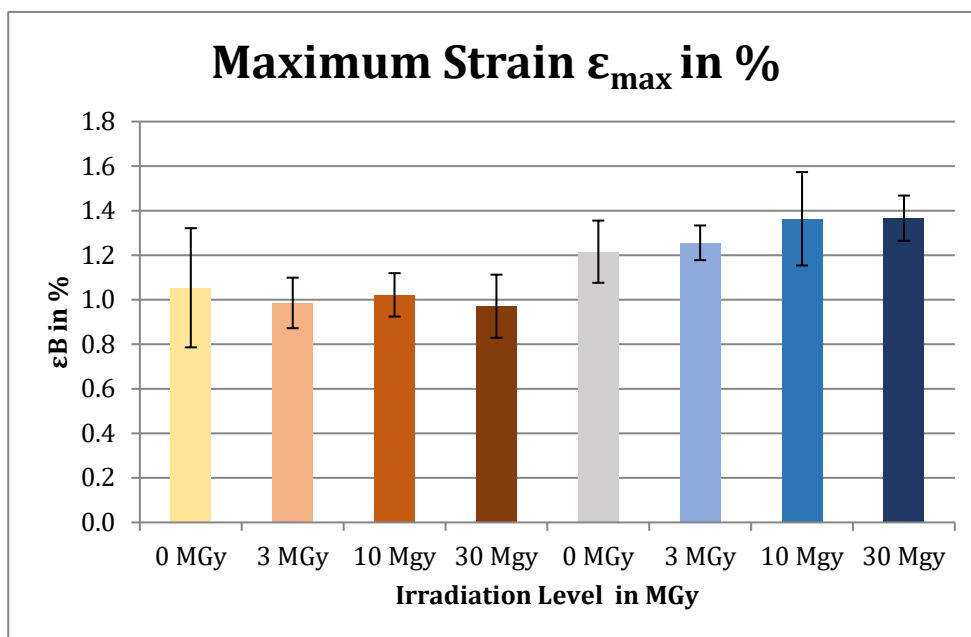Figure A.1.2. E-Module in GPa, measured by Airbus.

Figure A.1.3. Elongation in % at maximum stress, measured by Airbus.

A.2 Graphs of the Mechanical Testing

Stress-strain curves of #A0 top, #A0 mid, #A0 bot, #A3, #A10 and #A30 are shown in Figure A.2.1. The legends are listed in this order.

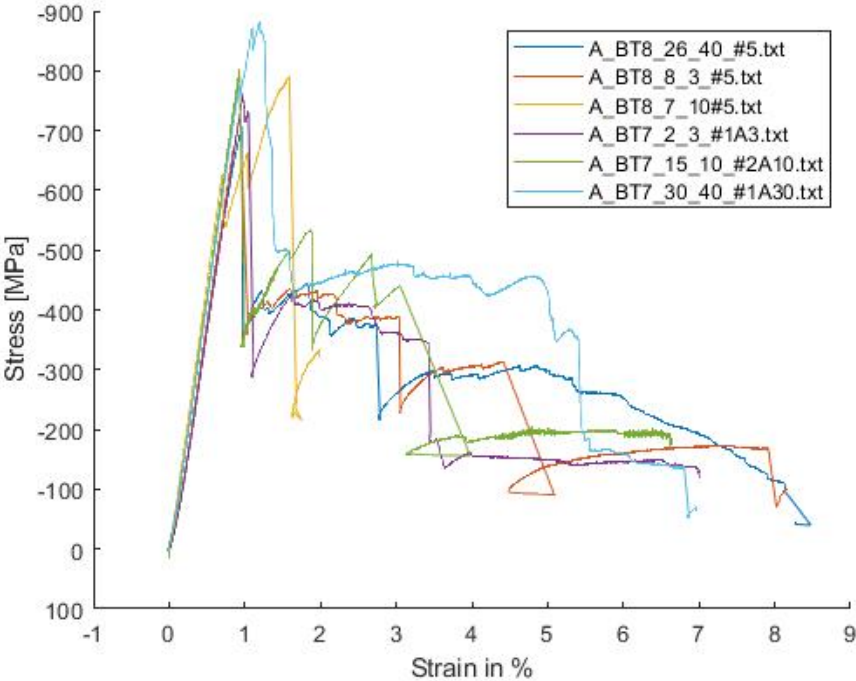**Figure A.2.1. Stress-strain curve for type A.**

Stress-strain curves of #B0 top, #B0 mid, #B0 bot, #B3, #B10 and #B30, see Figure A.2.2. The legends are listed in this order.
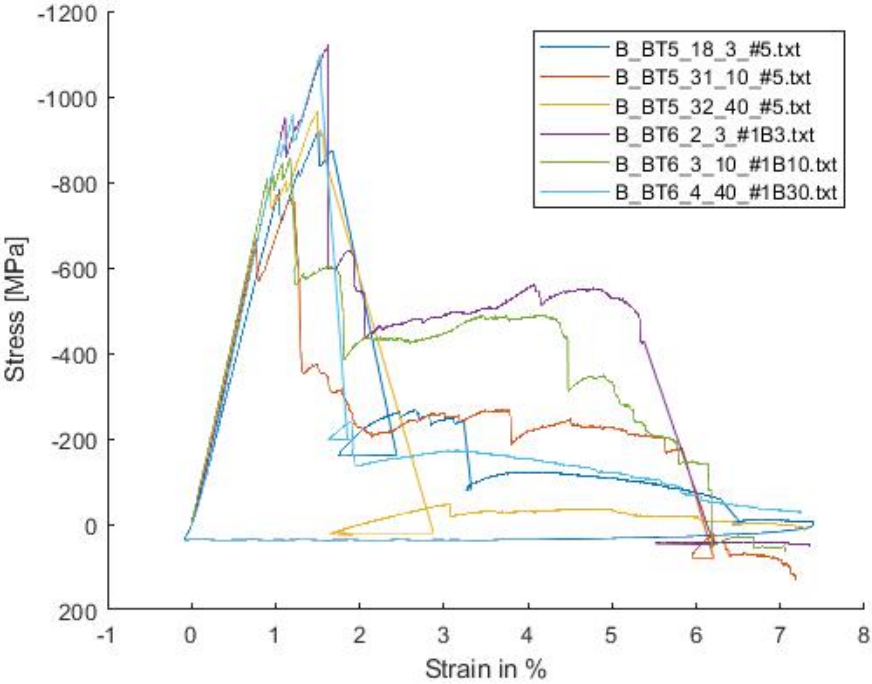

Figure A.2.2. Stress-strain curve for type B.

Force-deflection curves of #A0 top, #A0 mid, #A0 bot, #A3, #A10 and #A30. The legends are listed in this order.
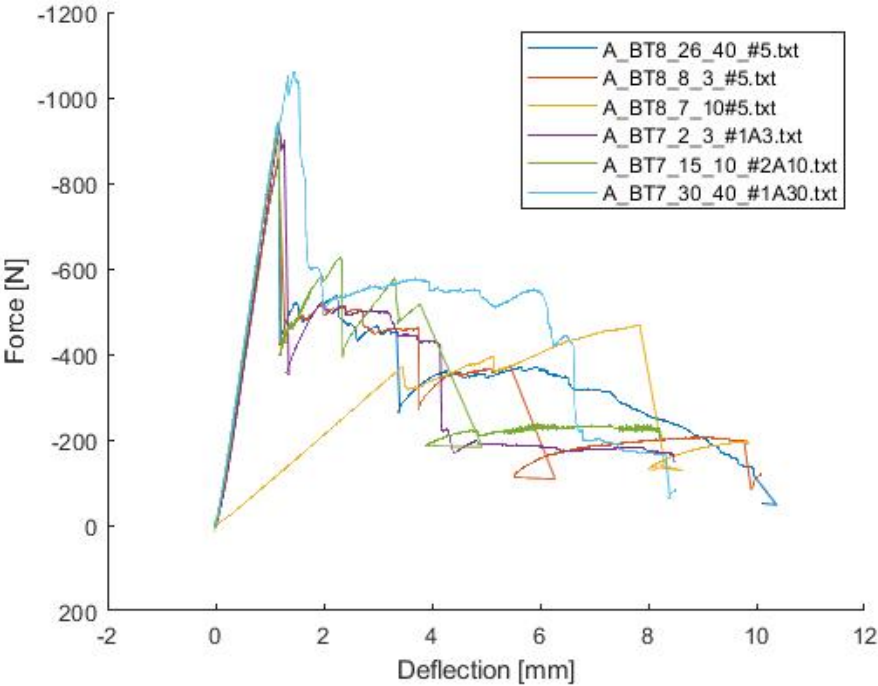
Figure A.2.3. Force-deflection curve for type A.

Force-deflection curves of #B0 top, #B0 mid, #B0 bot, #B3, #B10 and #B30. The legends are listed in this order.
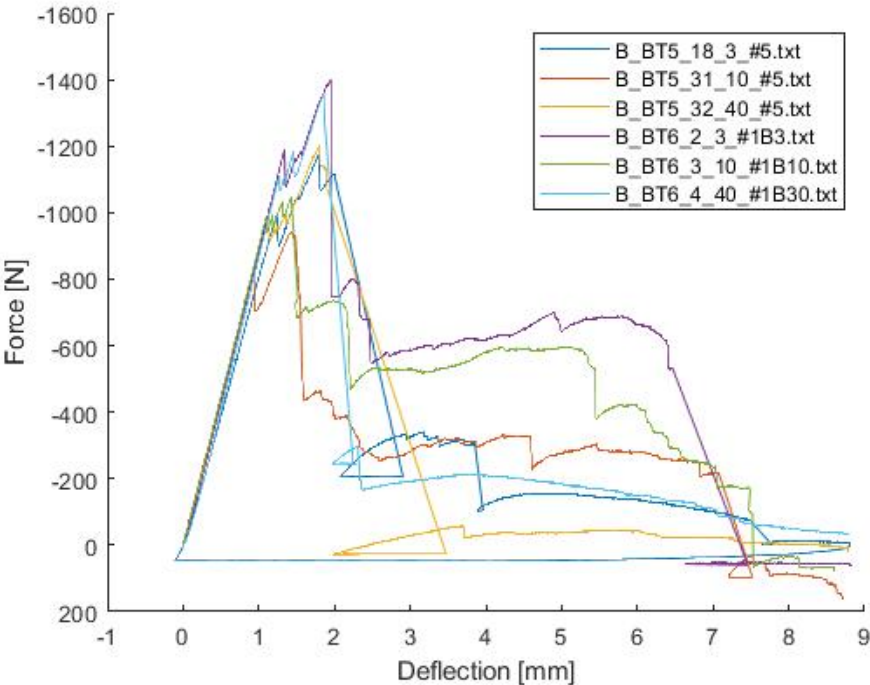
Figure A.2.4. Force-deflection curve for type B.

A.3 Correlation of Maximum Stress to Number of Pores

The correlation of maximum stress to number of pores at each diameter interval for each composite type is showed in Figure A.3.1 and Figure A.3. 2.
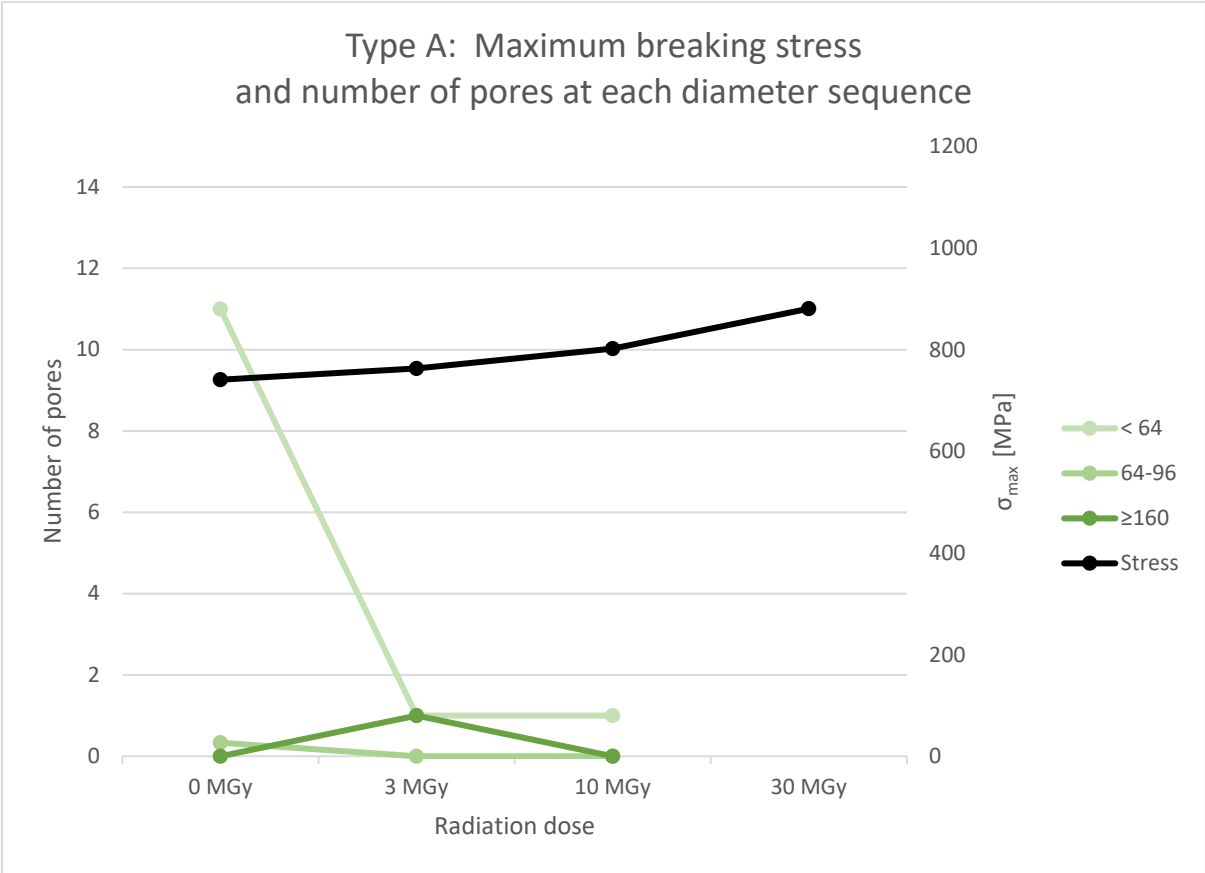
Figure A.3.1. Maximum stress to number of pores in different diameter sequences in type A.
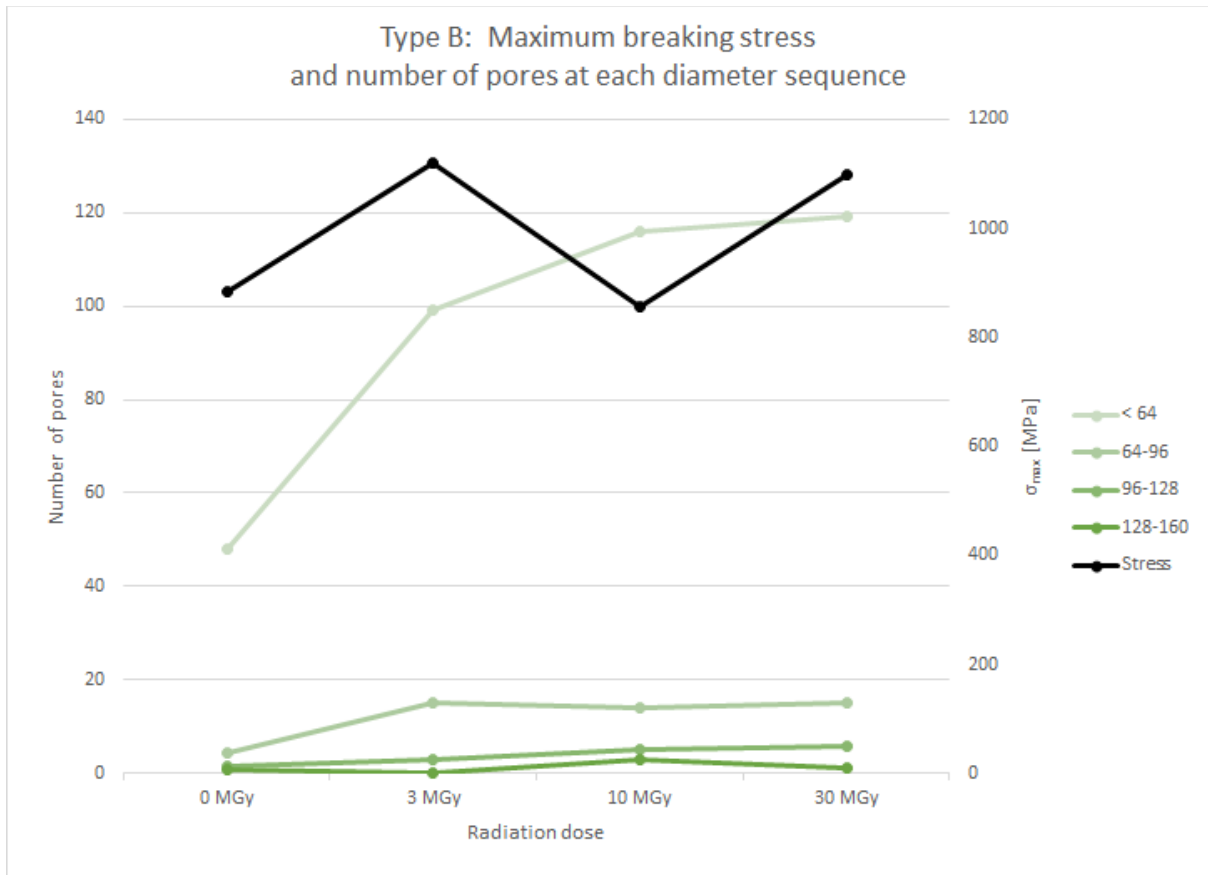
Figure A.3.2. Maximum stress to number of pores in different diameter sequences in type B.

A.4 Scanning Electron Microscope

The images from the SEM are shown in Figure A.4. 1 to Figure A.4.9.

mag	HFW	WD	det	HV	curr	spot	dwell	400 µm
100 x	1.49 mm	10.0 mm	LFD	10.00 kV	21 pA	4.0	120 µs	Materialteknik, LTH

Figure A.4.1. Fracture surface of #A0, at a magnification of 100 times.

mag	HFW	WD	det	HV	curr	spot	dwell	⊢ 50 μm ⊣
500 x	298 μm	10.0 mm	LFD	10.00 kV	21 pA	4.0	120 μs	Materialteknik, LTH

Figure A.4.3. Fracture surface of #A0 at a magnification of 500 times

mag	HFW	WD	det	HV	curr	spot	dwell	⊢ 50 μm ⊣
500 x	298 μm	10.8 mm	LFD	10.00 kV	21 pA	4.0	120 μs	Materialteknik, LTH

Figure A.4.2. Fracture surface of #A0, at a magnification of 500 times.

Figure A.4.5. Fracture surface of #A30 at a magnification of 500 times.

Figure A.4.4. Fracture surface of #B0 at a magnification of 500 times.

Figure A.4.6. Fracture surface of #B30 at a magnification of 500 times.

Figure A.4.7. Fracture surface of #B30 at a magnification of 500 times.
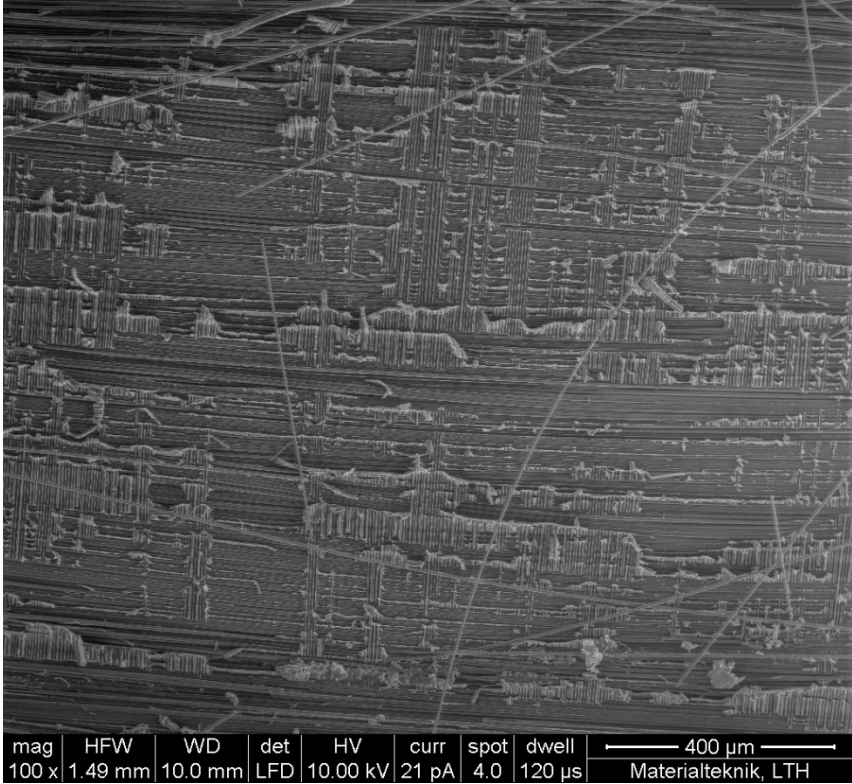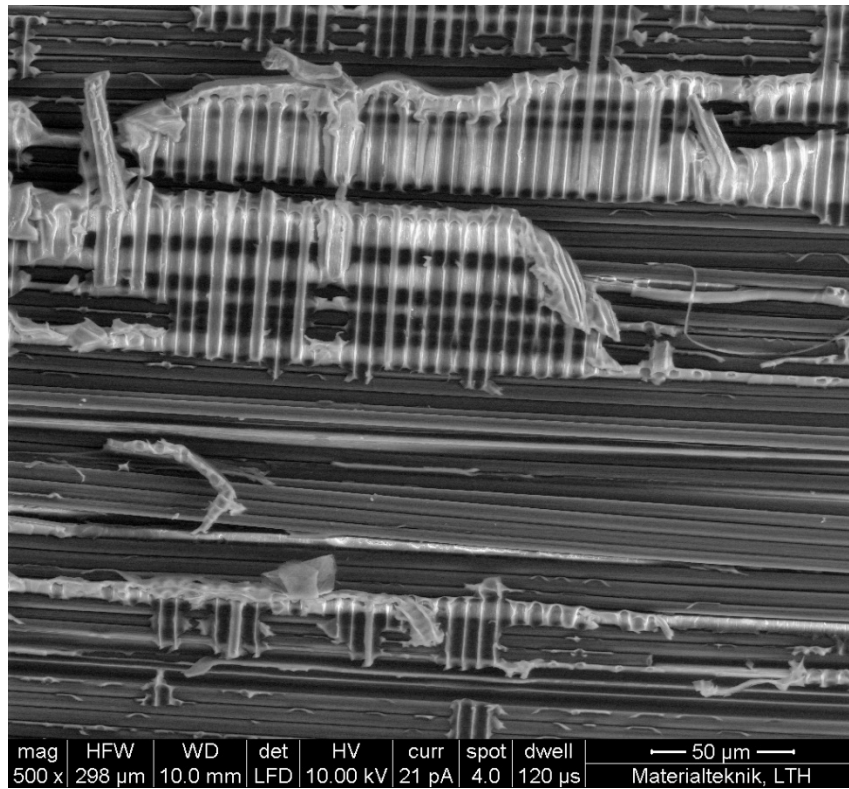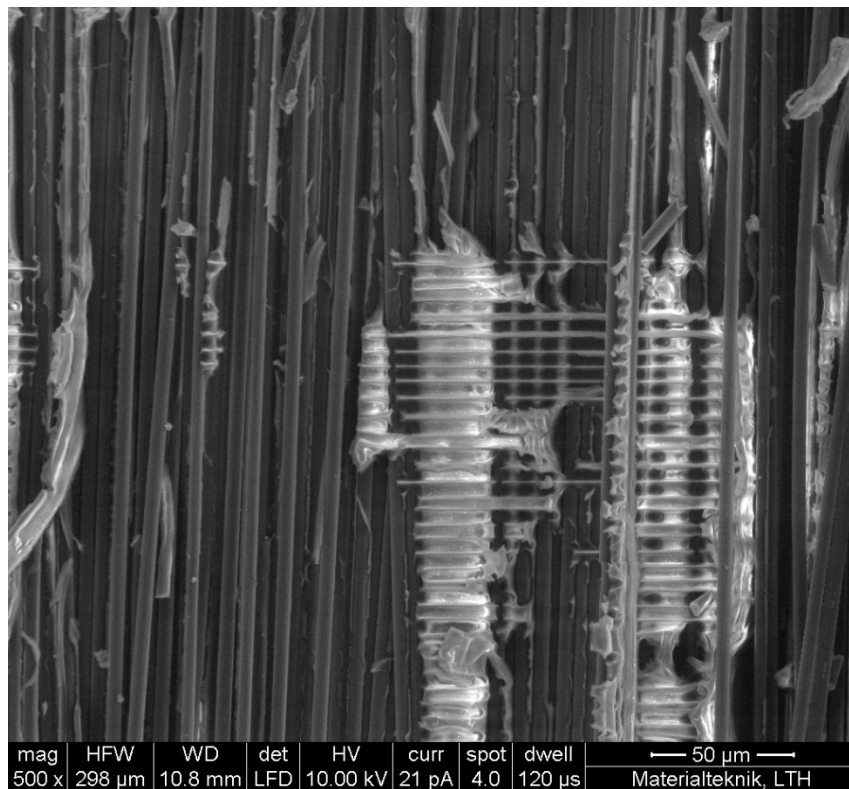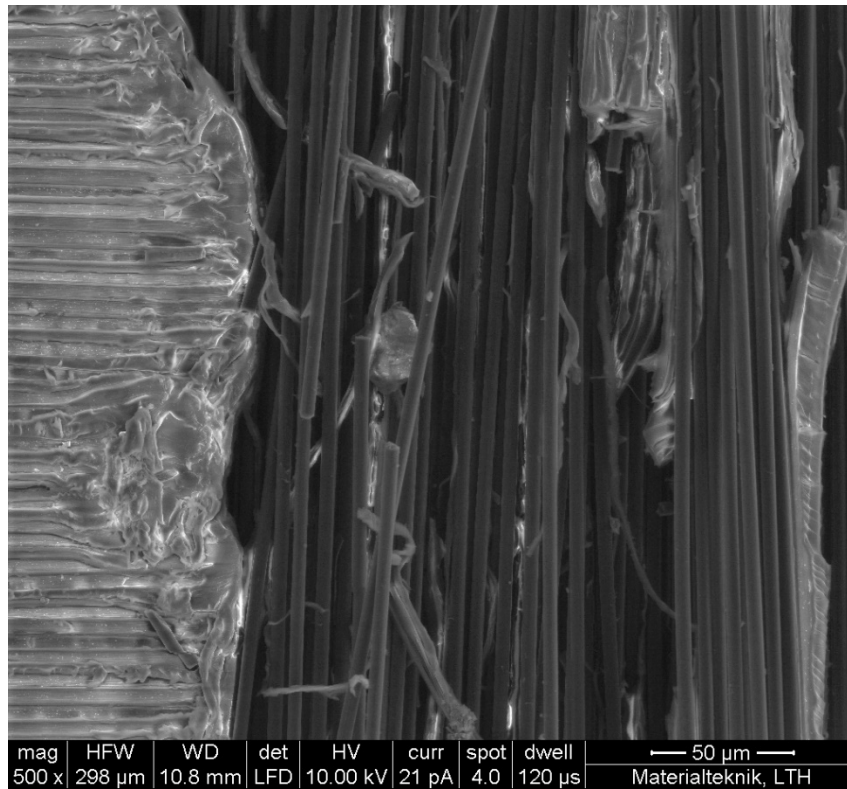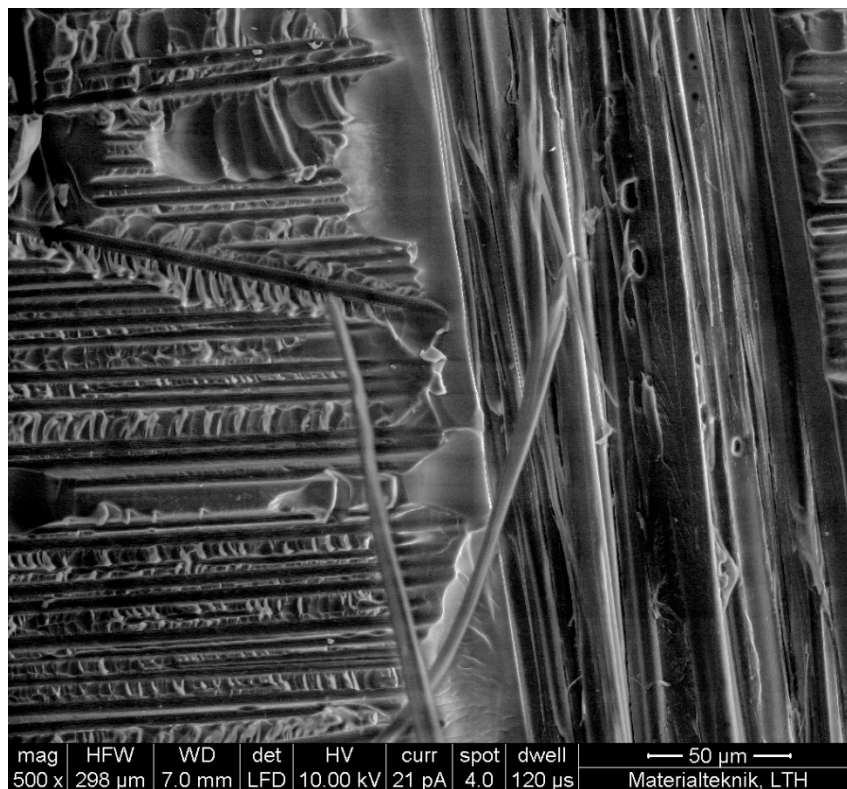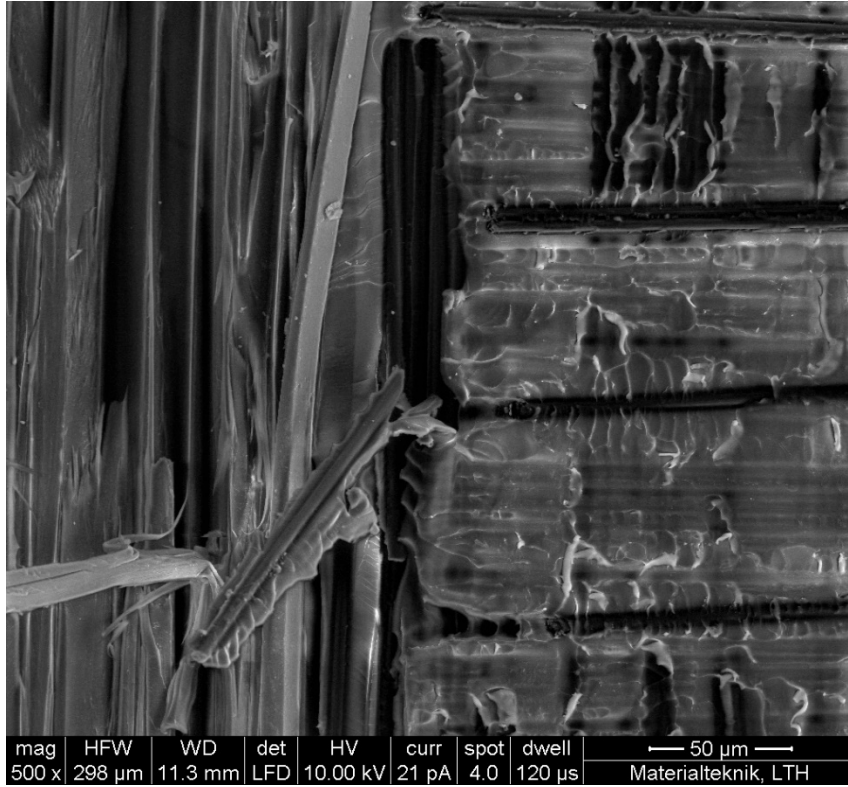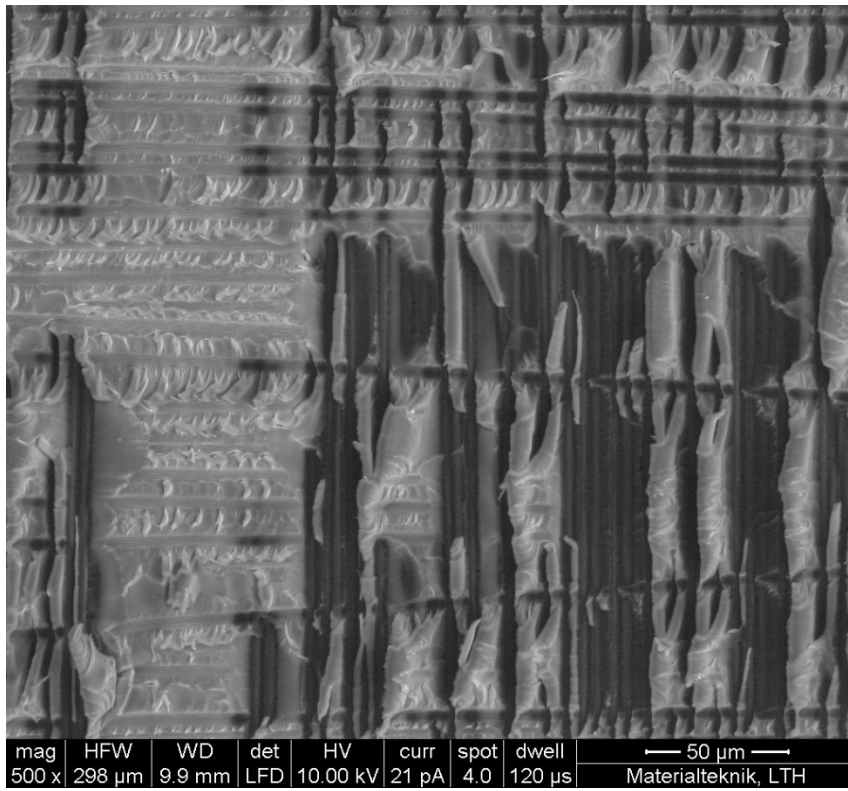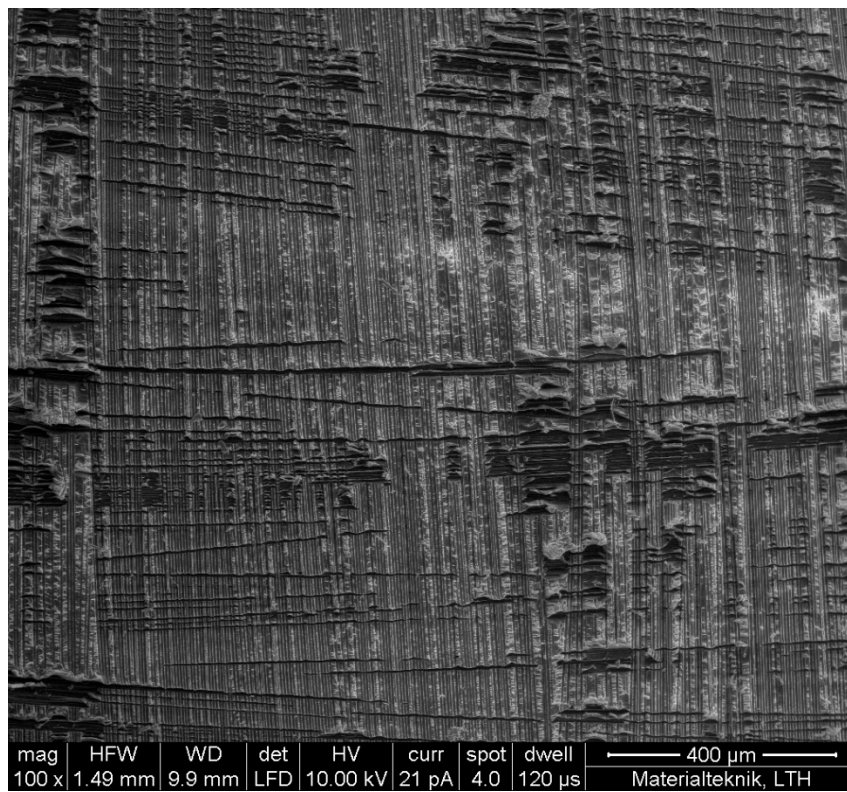
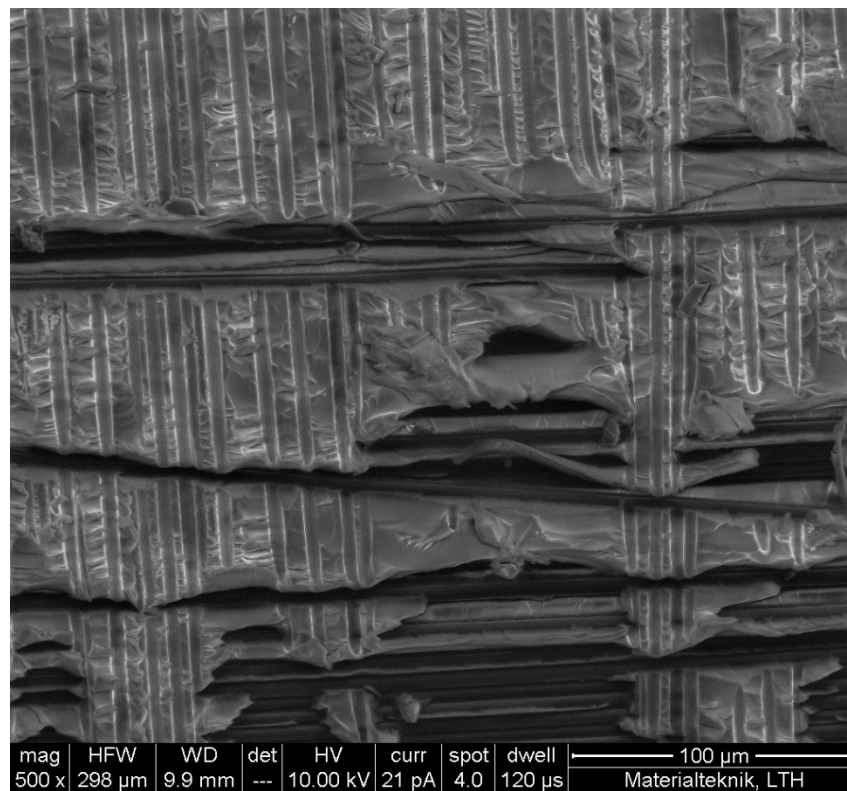**Figure A.4.8.** Fracture surface of #B10 at a magnification of 100 times.

Figure A.4.9. Fracture surface of #B10 at a magnification of 500 times.

11. Appendix B: MATLAB script

B.1 Cropping Samples

```matlab
close all
clear all
clc

%TYPE A UNIRRADIATED:
path = 'A0'; % Name of folder with uncropped specimens
path1 = 'A0_TOP'; % Name of folder with the cropped top specimen
path2 = 'A0_MID'; % Name of folder with the cropped middle specimen
path3 = 'A0_BOT'; % Name of folder with the cropped bottom specimen

% Since the specimens cover all of the columns, only rows need to be cropped. This is done by
using ImageJ to obtain the rows of the specimens at the first and last image in the image stack.

% TYPE A0 0150:
% The first row of the top specimen of the first image in the stack:
ptop_start1 = 38;
% The last row of the top specimen of the first image in the stack:
ptop_end1= 174;
% The number of rows of the top specimen of the first image in the stack:
ptop_diff = ptop_end1 - ptop_start1;


% The first row of the middle specimen of the first image in the stack:
pmid_start1 = 180;
% The last row of the middle specimen of the first image in the stack:
pmid_end1= 317;
% The number of rows of the middle specimen of the first image in the stack:
pmid_diff = pmid_end1 -pmid_start1;


% The first row of the bottom specimen of the first image in the stack:
pbot_start1 = 317;
% The last row of the bottom specimen of the first image in the stack:
pbot_end1= 451;
% The number of rows of the bottom specimen of the first image in the stack
pbot_diff = pbot_end1 -pbot_start1;

% TYPE A0 0850:
% The first row of the top specimen of the last image in the stack:
ptop_start2 = 45;
% The last row of the top specimen of the last image in the stack, making sure that the sample
is as thick as in the first image:
ptop_end2= ptop_start2 + ptop_diff;

% The first row of the middle specimen of the last image in the stack:
pmid_start2 = 188;
% The last row of the middle specimen of the last image in the stack, making sure that the
sample is as thick as in the first image:
pmid_end2= pmid_start2 + pmid_diff;
```

```matlab
% The first row of the bottom specimen of the last image in the stack:
pbot_start2 = 323;
% The last row of the bottom specimen of the last image in the stack, making sure that the
sample is as thick as in the first image:
pbot_end2= pbot_start2 + pbot_diff;


% One picture at a time is imported from the folder with uncropped specimens and each sample is
cropped into separate folders. However, since the samples are tilting, the horizontal position
is disrupted for each image. This is corrected by using "linint", see section B.1.1 Linint which
uses linear interpolation to adjust the crop section.

imstart=150;
imend=850;

for i = imstart:imend

    data(:,:)= imread(strcat( path, '\' ,'0',num2str(i),'.tiff'));
    im = i;
    y_top_start = round(linint(imstart, imend, ptop_start1, ptop_start2, im));
    y_top_end = round(linint(imstart, imend, ptop_end1, ptop_end2, im));

    y_mid_start = round(linint(imstart, imend, pmid_start1, pmid_start2, im));
    y_mid_end = round(linint(imstart, imend, pmid_end1, pmid_end2, im));

    y_bot_start = round(linint(imstart, imend, pbot_start1, pbot_start2, im));
    y_bot_end = round(linint(imstart, imend, pbot_end1, pbot_end2, im));

    crop_top = data(y_top_start:y_top_end, :);
    crop_mid = data(y_mid_start:y_mid_end, :);
    crop_bot = data(y_bot_start:y_bot_end, :);


 % The different samples are placed in separate folders

    imwrite(crop_top, strcat( path1, '\' ,'0',num2str(i),'.tiff'));

    imwrite(crop_mid, strcat( path2, '\' ,'0',num2str(i),'.tiff'));

    imwrite(crop_bot, strcat( path3, '\' ,'0',num2str(i),'.tiff'));

end
```

B.1.1 Linint

```matlab
function [pixel] = linint(imstart, imend, pstart, pend, im )
%Linear interpolation
      pixel = pstart + (im-imstart) *(pend-pstart)/(imend-imstart);
end
```

B.2 Porosity Analysis

```
clear all
close all
clc

path1 = 'A0_top';
path2 = 'A0_mid';
path3 = 'A0_bot';
d_top = [];
d_mid = [];
d_bot = [];
j=0;

% Imports each image, i.e. all pixel values, of each sample into separate matrices d_top, d_mid
and d_bot:

imstart=150;
imend=850;
for i = imstart:imend
    j= i-imstart+1;

    d_top(:,:,j)= imread(strcat( path1, '\' ,'0',num2str(i),'.tiff'));
    d_mid(:,:,j)= imread(strcat( path2, '\' ,'0',num2str(i),'.tiff'));
    d_bot(:,:,j)= imread(strcat( path3, '\' ,'0',num2str(i),'.tiff'));

end

% The matrices are then analysed by the function "PoreFinder", see B.2.1 PoreFinder:

ls_top = PoreFinder(d_top);
ls_mid = PoreFinder(d_mid);
ls_bot = PoreFinder(d_bot);

% The extracted information is then converted to a csv file to facilitate construction of graphs.

csvwrite('TypeB3.csv',ls_top)
csvwrite('TypeB10.csv',ls_mid)
csvwrite('TypeB30.csv',ls_bot)
```

B.2.1 PoreFinder

```
function [ls] = PoreFinder(data)
% Detects pores in the samples

        % Determines number of rows, columns and images:
        [nbr_rows nbr_col nbr_images] = size(data);

        % Makes a vector out of all grey scale values of all the voxels in the image stack, using
        "makeVoxels" described in B.2.1.1 MakeVoxels:

        voxels = makeVoxels(data);
        % Plots histogram of grey scale values
        histogram(voxels)

        % The threshold value is manually detected in the histogram as described in section 5.3
        and the value is then entered in the binarisation function, see section B.2.1.2
        Binarisation:
        data2= Binarisation(data, 1700);
```

```
% To make sure that the binarisation works, it is tested on an image which is known to
include a pore. In this case, it's image number 588 in the stack:
imshow(data2(:,:,588));

% When the accuracy of the binarisation is confirmed, an existing MATLAB function
"bwconncomp" is used. This function connects pixels in different ways depending on the
number after the comma. In this case the number after the comma is 6, meaning that this
function connects the voxels if their faces touch. Bwconncomp returns both number of
voxels in each defect but also the number of areas found.

CC = bwconncomp(data2,6);

% Another existing function in MATLAB, "labelmatrix" is used to label the CC-matrix:

L = labelmatrix(CC);

% To measure properties of 3-D volumetric image regions, an existing MATLAB function
called "regionprops3" can be used. Regionprops3 measures a set of properties for each
connected component In the L-matrix:

stats = regionprops3(L, 'Volume', 'Centroid', 'EigenValues', 'EquivDiameter');

% Using certain limits, the information from regionprops3 is then used as an input in
section B.2.1.3 getTable, which prints a table of all the information needed of potential
pores.
RatioLimit = 0.00;
VolumeMin = 2;
VolumeMax = 10000;

[prop, ls] =getTable(nbr_rows, stats, RatioLimit, VolumeMin, VolumeMax);

end
```

B.2.1.1 MakeVoxels

```
function [ x ] = makeVoxels( I )
    % Makes a vector out of all grey scale values of all the voxels in the image stack using
    an existing function "reshape".
    [len1 len2 len3 ]=size(I);

    x = reshape(I,1,len1*len2*len3);

end
```

B.2.1.2 Binarisation

```
function [ new_image ] = Binarisation( image, threshold )
%Sets values above the threshold value to 0, and the rest to 50100.

    new_image = image;

    new_image(new_image>threshold) = 32000;
    new_image(new_image<threshold) = 50100;
    new_image(new_image==32000) = 0;

end
```

B.2.1.3 getTable

```matlab
function [area, ls] = getTable(nbr_rows, stats,RatioLimit,VolumeMin, VolumeMax)
% Prints a table of information of the detected pores in the sample. This functions also returns
a matrix with this information.

        % Extracts the information measured previously using regionprops3:

        volume = stats.Volume;
        coordinates = stats.Centroid;
        diameter = stats.EquivDiameter;
        EigenValues = stats.EigenValues;
        [Len1 Len2]= size(volume);
        ls=[];

        % Prints the heading of the table
        fprintf('start of area printing:\n\n');
        fprintf('%8s %18.6s %18.6s %18.6s %18.6s %18.6s %18.6s %18.6s %18.6s','x,y,z',
        'Eigen1', 'Eigen2', 'Eigen3','Volume', 'D', 'Ratio', 'Pore');
        fprintf('\n');

        % An empty matrix "area" is created:
        area = zeros(Len1,8);

        % For each detected pore, the script filters out the first 10 and the last 5 rows to
        guarantee that the script does not detect the background as a pore:
        for i = 1: Len1

                area(i,4) = volume(i);
                if (coordinates(i,2) < 10) || (coordinates(i,2) > (nbr_rows-5))
                    continue
                end

                % xyz corresponds to the coordinates of the pore:
                xyz           =           strcat(          '(',          num2str(coordinates(i,1),
                '%18.0f')),',',num2str(coordinates(i,2),                 '%18.0f')),',',
                num2str(coordinates(i,3),'%18.0f'), ')');

                area(i,1) = EigenValues{i}(1);
                area(i,2) = EigenValues{i}(2);
                area(i,3) = EigenValues{i}(3);
                area(i,5) = diameter(i);


                % The ratio of the minimum and maximum axis of the pore is calculated to get an
                idea of the shape of the pore:
                area(i,6) = area(i,3)./ area(i,1) ;

                % If the detected pore is within the limits, it is marked with a "1" in the table
                and then the table is printed:

                if area(i,6) >= RatioLimit
                    area(i,7) = 1;
                end

                        if (area(i,4) > VolumeMin) && (area(i,4) < VolumeMax)

                        area(i,8)=1;

                        fprintf('%12s %18.2f %18.2f %18.2f %18.2f %18.2f %18.2f %18.2f\n',xyz,
                        area(i,1),    area(i,2),    area(i,3),area(i,4),area(i,5),    area(i,6),
                        area(i,8));
```

```matlab
                ls =[ls; area(i,1),area(i,2), area(i,3),area(i,4),area(i,5), area(i,6),
                area(i,8)];

             end
      end
end
```